Politecnico di Milano

School of Industrial and Information Engineering
Master of Science (MSc) in
Materials Engineering and Nanotechnology

"A feasibility study into implementation of nanoporous ZnO as the photoanode in Perovskite based solar cell"

Supervisor: Professor Carlo Spartaco Casari

Micro and Nanostructured Materials Lab., Energy Department, Politecnico di Milano, www.nanolab.polimi.it

Co-supervisor: Dr. Annamaria Petrozza

Center for Nanoscience and Technology, Italian Institute of Technology (IIT), http://cnst.iit.it

Co-supervisor: Dr. Piero Mazzolini

Micro and Nanostructured Materials Lab., Energy Department, Politecnico di Milano, www.nanolab.polimi.it

Thesis by: ***Aryan Chalay Amoly***

Student Number (Matricola): ***801309***

Academic year, 2014-2015

Acknowledgments

I would like to express my gratitude to Professor Carlo Spartaco Casari, Dr. Piero Mazzolini and my colleagues from Italian Institute of Technology (IIT) who all provided me with invaluable insight and expertise that greatly assisted this project.

Furthermore, I am immensely grateful to Diritto allo Studio (Borse di studio) whose financial support for my entire MSc degree enabled me to accomplish my educational goals as I always dreamed about.

Dedicated to
my lovely parents
for their endless support and encouragement

“Everything you can imagine is real.”

— Pablo Picasso

Table of contents

List of Figures

List of Tables

Abstract

Perovskite based solar cells (PerovCells) have become one of the hot topics within the renewable energies field during last five years. PerovCell offers a combination of promising advantages including but not limited to ease of fabrication, strong solar absorption and low non-radiative carrier recombination rates in addition to relatively high power conversion efficiencies (PCE). However, the material selection for different layers, optimal cell design and fabrication methods for such a novel solar cell are all still under vast research and study for successful development and commercialization of PerovCells in the near future.

In this project, a systematic study of pulsed laser deposition (PLD) fabricated hierarchical ZnO photoanode was carried out to shed light on the novel candidate PerovCell fabrication protocol.

PLD parameters including deposition duration and background oxygen pressure were optimized to attain the favorable ZnO film thickness and degree of porosity, respectively. We demonstrated that 10 and 300Pa oxygen pressures are suitable to make the desirable compact and nanoporous ZnO films, respectively. Perovskite solution was subsequently spin coated on ZnO films and annealed at 100°C for various durations. Our findings suggested a significantly short annealing time (about 15±5 seconds) is already sufficient to form the perovskite film.

Morphology and structure of perovskite and ZnO films were investigated by scanning electron microscopy (SEM) and Raman spectroscopy, while photoluminescence and absorption spectra were employed to uncover optical properties of perovskite sensitized ZnO substrates. The devices were fabricated according to the obtained optimized conditions adopting the state-of-the-art PerovCell oriented stack of layers; the efficiency and performance of the devices were evaluated by means of solar simulator. Finally, we related the cell operation to the fundamental properties of the constituent materials.

Sommario

Nel campo delle celle solari di nuova generazione, le celle solari basate sull'utilizzo delle perovskiti come materiale attivo (PerovCells) si sono rivelate come una tra le più promettenti tecnologie emergenti. Il motivo principale è legato al loro straordinario sviluppo in termini di efficienza negli ultimi 5 anni. Inoltre, le PerovCells sembrano poter garantire facili processi di fabbricazione, con conseguenti bassi costi associati. Le ragioni legate alle loro performance superiori sono legate ad un elevato assorbimento nello spettro solare, un basso tasso di ricombinazione delle cariche generate e ad un'ottima efficienza di conversione energetica in termini di potenza. Nonostante tutto, trattandosi di una nuova tecnologia emergente, la scelta dei diversi materiali costituenti la cella solare e l'ottimizzazione dei processi di produzione associati costituiscono argomento di studio di elevato interesse nel campo della ricerca, in quanto punti cardine per la futura commercializzazione dei dispositivi.

In questa tesi, si presenta uno studio sistematico di fotoanodi di ossido di zinco (ZnO) aventi struttura gerarchica ottenuta tramite deposizioni a laser pulsato (PLD).

I parametri di deposizione tramite PLD saranno argomento di studio approfondito di questa tesi (pressione di deposizione, tempo di durata, grado di porosità ottenuto). Si dimostrerà che la struttura più adatta per la realizzazione di celle si basa sulla deposizione di uno strato poroso depositato a 10 Pa di ossigeno, seguita da uno strato ad elevata porosità ottenuto ablando il materiale ad una pressione parziale di 300 Pa. La soluzione di precursori di perovskite è stata successivamente applicata sui film di ZnO con la tecnica di spin coating; la cristallizzazione della perovskite stessa è stata ottenuta tramite trattamento termico successivo alla temperatura di 100°C. Si è studiato il tempo necessario all'ottenimento di una cristallizzazione ottimale; i risultati riportati dimostrano come i tempi necessari siano di breve durata (circa 15 ± 5 secondi). La morfologia e la struttura della perovskite così ottenuta e dei film sottili di

ZnO sono state studiate tramite microscopia a scansione elettronica (SEM) e spettroscopia Raman, mentre spettri di fotoluminescenza e di assorbimento sono stati utilizzati per studiare le proprietà ottiche associate alle strutture composite ZnO + perovskite. Alla fine del lavoro di ottimizzazione sono state fabbricate delle celle solari, il cui funzionamento è stato testato al simulatore solare. Si cercherà di legare i valori ottenuti dalle celle fabbricate con le proprietà fondamentali dei materiali che la costituiscono.

Introduction

Solar energy, as a clean and vast energy source, is widely believed to be a promising way to address the global energy crisis and environment pollution. Among various known solar cell techniques, ones offering both relatively high power conversion efficiencies (PCE) and low processing costs are of superior importance. A new generation of mixed organic–inorganic halide perovskite based photovoltaics (here on PerovCells) offers tantalizing prospects on both fronts. Last five years have seen a rapidly growing understanding of each individual layer of PerovCells and optimal cell designs.

Excitonic PVs in general are made of light absorber layer (here Perovskite) sandwiched between hole transport material (HTM) and electron transport material (ETM) or so called photoanode. A number of studies have been directed to uncover favorable HTM and ETM layers for PerovCells in terms of material type and structural characteristics. HTM, just as the name implies, transports the holes to the back electrode when the excitons are dissociated into electrons and holes. Solid state Tris(bis(trifle-oromethylsulfonyl)imide)] added spiro-OMeTAD is believed to be the most suitable HTMs for PerovCells. The latter HTM material offers a combination of high electron life time and fast charge transport resulting in improved solar cell performance [1].

Photoanodes, as the support for sensitizer loading, play a vital role in the performance of PerovCells. So far, several kinds of photoanodes have been utilized, including TiO_2, Al_2O_3 [2] as well as ZnO [3]. As regards the structural characteristic of photoanodes, studies have suggested the potentials of nanoparticle, one-dimensional nanomaterial and planar photoanode structures to be exploited in PerovCells [4].

The vacuum energy levels (valence and conduction bands edge) of ZnO and TiO_2 correspond to almost the same values resulting in similar energy band gap as high as 3.2ev. Nevertheless, ZnO offers a number of advantages over TiO_2 which makes it a promising photoanode to be further investigated for use in

PerovCells. ZnO is known to have an electron mobility that is substantially higher than that of TiO_2 [5]. Moreover, ZnO nanoparticle layer can be deposited easily by spin coating and requires no heating or sintering step unlike nanoparticle TiO_2 which requires sintering at 500°C for 1h prior to use rendering it incompatible with flexible substrates [3]. ZnO photoanode implemented perovskite solar cell exhibited promising efficiency as high as 15.7% [3]. PerovCells on flexible substrates can be substantially advantageous for portable electronic devices (such as cell phones and laptops) as an unbreakable platform for the devices whose batteries can be charged upon sun radiation exposure.

Furthermore, it was shown by De Bastiani et. al. [6] that spin coated perovskite on ZnO nanoparticle photoanode layer requires annealing in the range of 1min at 100°C, while annealing time for perovskite sensitized TiO_2 nanoparticle layer has been well established to be about 60min at 100°C [7]. In the large-scale photovoltaics fabrication, lower time and temperature processing of PVs constituted materials plays an imperative role to attain the highest economical added value as possible.

Unique potentials of ZnO as photoanode material presenting high electron mobility, its feasibility for flexible solar cell fabrication, significantly short perovskite annealing time necessity in addition to its similar vacuum energy levels with respect to the conventionally used photoanode, TiO_2, renders it an interesting candidate for large-scale PerovCells fabrication.

Above all, hierarchical photoanode structure fabricated by pulsed laser deposition has already promised great potentials to be utilized in dye sensitized solar cells [8, 9]. Hierarchical photoanode is well established to increase the electron lifetime (so better charge collection efficiency) [8]. Furthermore, hierarchical architecture combines the efficient light harvesting and increased surface area for dye absorption, all beneficial for cell operation [4]. Nevertheless, PLD fabricated hierarchical structure has never been studied as photoanode in PerovCells.

Accordingly, in this project, a systematic study of PLD-fabricated hierarchical ZnO as the photoanode in PerovCells was carried out to shed light on novel candidate perovskite solar cell fabrication protocol.

1-Photovoltaics

1-1-Renewable energy significance

The fossil fuels, such as coal, oil and natural gas, have been the world's main energy supply from several centuries ago, up to now. However, the reservoirs of these non-renewable resources are limited, politically and geographically dependent, and this issue is considered as one of the main causes for the high prices of fossil fuels in recent years. Moreover, many of the present environmental problems, including global warming, climate change, and air pollution have been resulted from deleterious gas emissions associated with fossil fuels combustion [10]. Therefore, considering disadvantages and the limited reservoirs of fossil fuels, development of alternative sources of energy, renewable energy resources, is inevitable.

As shown in Figure 1, apart from fossil fuels, nuclear power and renewable energies (sourced from solar, wind, geothermal, hydroelectricity, and tide) considerably contribute to electricity generation too. Global perception of renewable energy has been shifted considerably since 2004; over the last years, continuing technology advances and rapid deployment of many renewable energy technologies have demonstrated that their potentials can be substantially achieved [11]. Figure 2 shows global investment in renewable energy during 2013 and highlights how fast solar power is boosting recently.

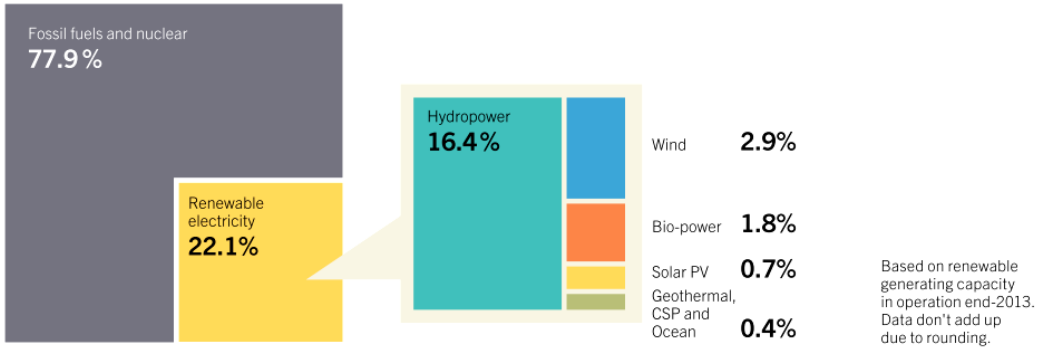

Figure 1: Estimated renewable energy share of global electricity production, end-2013 [11].

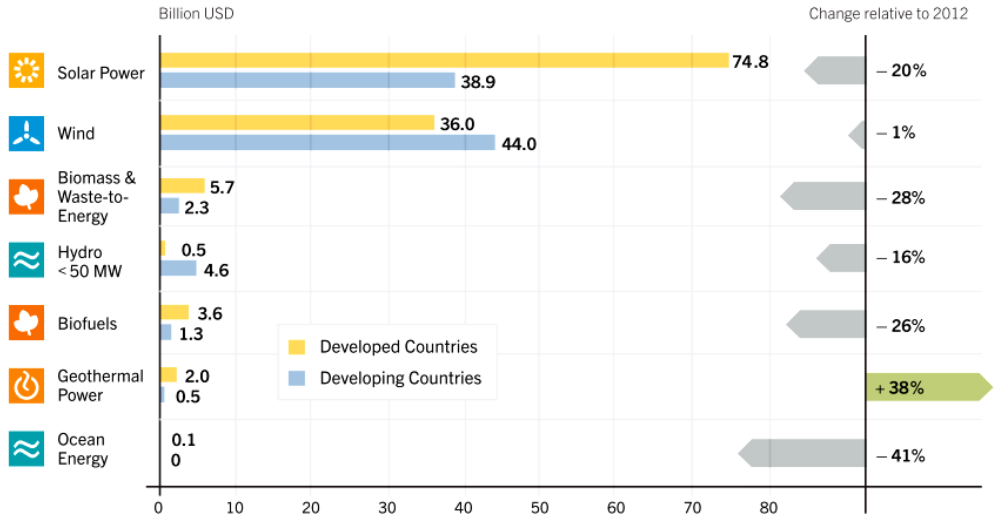

Figure 2: Global new investment in renewable energy by technology in developed and developing countries in 2013 compared to 2012 [11].

Among various renewable energies, photovoltaics (PV) are of high industrial importance thanks to unique advantages they offer [12], as follows:

- ✓ "Fuel" source (solar radiation) is vast, widely accessible and essentially infinite
- ✓ No emissions, combustion or radioactive waste
- ✓ Low operating costs (no fuel)
- ✓ No moving parts (no wear); theoretically everlasting
- ✓ Ambient temperature operation (no high-temperature corrosion or safety issues)
- ✓ High reliability of solar modules (manufacturers' guarantees over 30 years)
- ✓ Rather predictable annual output
- ✓ Can be integrated into new or existing building structures
- ✓ Can be very rapidly installed at nearly any point-of-use

According to the current available data, the solar photovoltaics market had a record year in 2013, adding more than 39 GW for a total exceeding 139 GW (See Figure 3a). As regards geographical PV advancement, China saw

spectacular growth, accounting for nearly one-third of global capacity added, followed by Japan and the United States (See Figure 3b). Solar PV is starting to play a substantial role in electricity generation in some countries, particularly in Europe, while lower prices are opening new markets from Africa and the Middle East to Asia and Latin America. Interest continued to grow in corporate- and community-owned systems, while the number and size of utility-scale systems continued to increase. Module prices have been stabilised, while production costs continued to fall and solar cell efficiencies increased steadily. Many manufacturers began expanding production capacity to meet expected further growth in demand [11].

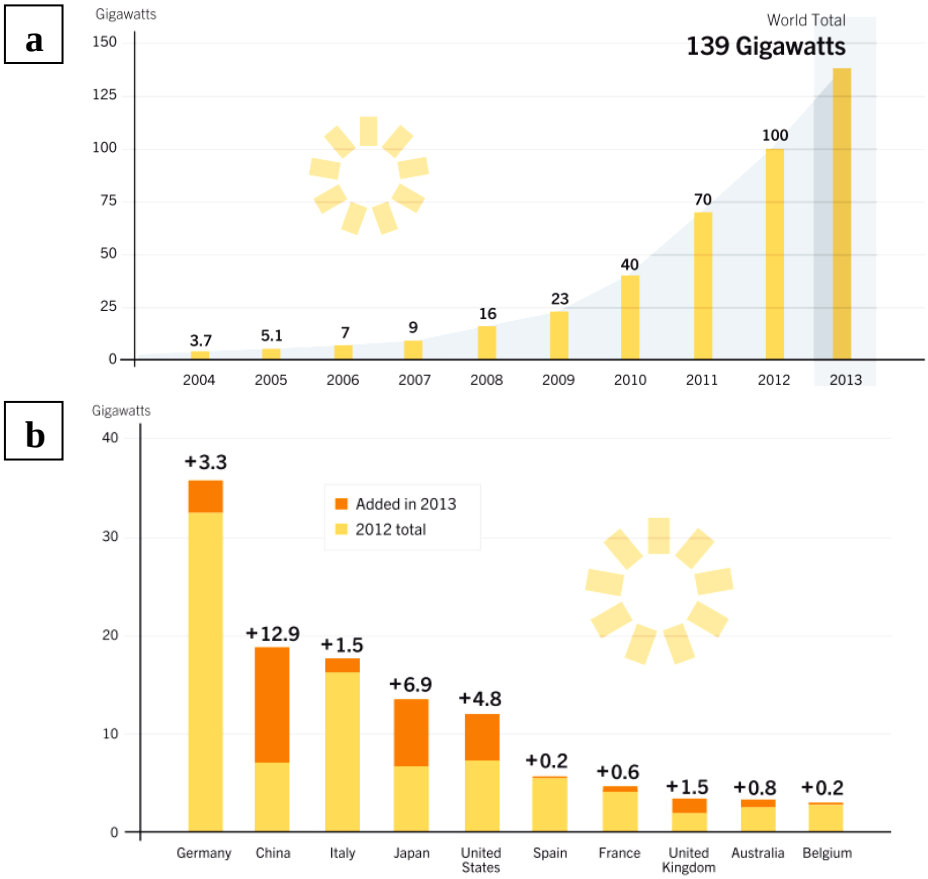

Figure 3: a) Solar PV total global capacity [11], b) Solar PV capacity and additions, top 10 countries [11].

1-2-The three generations of photovoltaics

Photovoltaics are typically categorized into three main generations, namely silicon based PV (I-generation), thin film PV (II-generation) and nanotechnology-enhanced PV (III-generation).

Single crystal wafer-based solar cell technology is considered as the first generation PV for terrestrial applications. As this technology has matured, total costs have become increasingly dominated by material costs, namely those of the silicon wafer, the glass cover sheet, and encapsulants. First-generation PV approach employs fabrication of high-quality, low-defect, single-crystal PV devices that have high efficiencies approaching the limiting efficiencies for single-bandgap devices but use energy- and time-intensive techniques.

In order to decrease the material costs of crystalline silicon solar cells, research has been directed toward developing low cost thin-film solar cells, which represent a second generation solar cells [12]. There are several semiconductor materials that are potential candidates for thin-film solar cells, namely Copper Indium Gallium diselenide ($CuInGaSe_2$=CIGS), Cadmium Telluride (CdTe), hydrogenated amorphous silicon (α-Si:H) and thin-film polycrystalline silicon (f-Si).

Third-generation approaches to photovoltaics aim to achieve high-efficiency devices but still keeping thin-film methods. Calculations based on thermodynamics demonstrate that the limit on the conversion efficiency of sunlight to electricity is 93% as opposed to the upper limit of 33% for a single junction solar cell, such as a silicon wafer and most present thin-film solar cells [12] (See Figure 4). This suggests that the performance of solar cells could be improved 2-3 times when different concepts were used to produce a third generation of high efficiency, thin-film solar cells [12]. Third-generation photovoltaics embraces different approaches such as multiple energy level approaches, multiple carrier excitation, hot carrier cells, modulation of the spectrum (up/down conversion), intermediate-level cells (impurity PV and

intermediate band solar cells), thin-film tandems, a-Si tandems, Si nanostructure tandems and implementing concentrator systems [13]. Furthermore, third-generation PVs include excitonic solar cells such as organic solar cells (e.g. polymer bulk heterojunctions, BHJ), Hybrid solar cells (polymer/oxide; polymer/QD), Dye-sensitized solar cells (DSSC), QD-sensitized solar cells as well as Perovskite based solar cells [14].

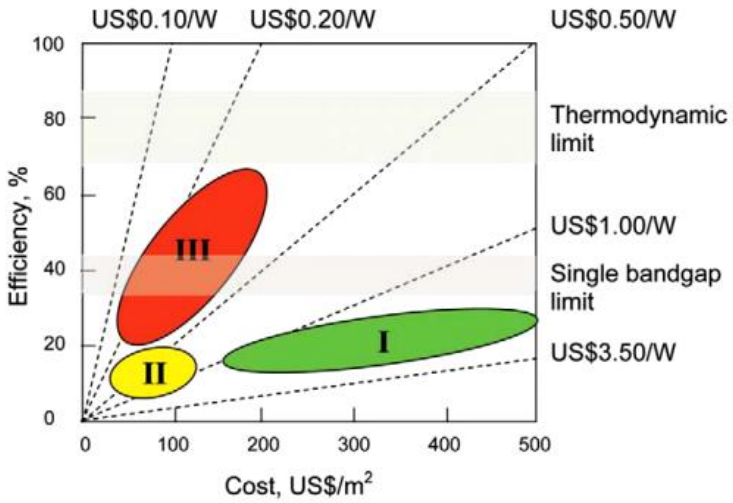

Figure 4: Efficiency and cost projections for first, second, and third- generation PV technologies.

Scholars throughout the world are constantly working on multiple aspects of solar cells so as to improve the final solar cells' efficiency. The highest record efficiencies obtained for laboratory-scale solar cells of different types are chronologically summarized in the Figure 5, collected by NREL [15]. It should be taken into account that commercially available solar cells, are often less efficient compared to the records due to manufacturing complexities on a large scale. Although multi junction (equipped with illumination concentrator) PVs show the highest record efficiencies, crystalline and multicrystalline silicon PVs still possess the biggest share of the market.

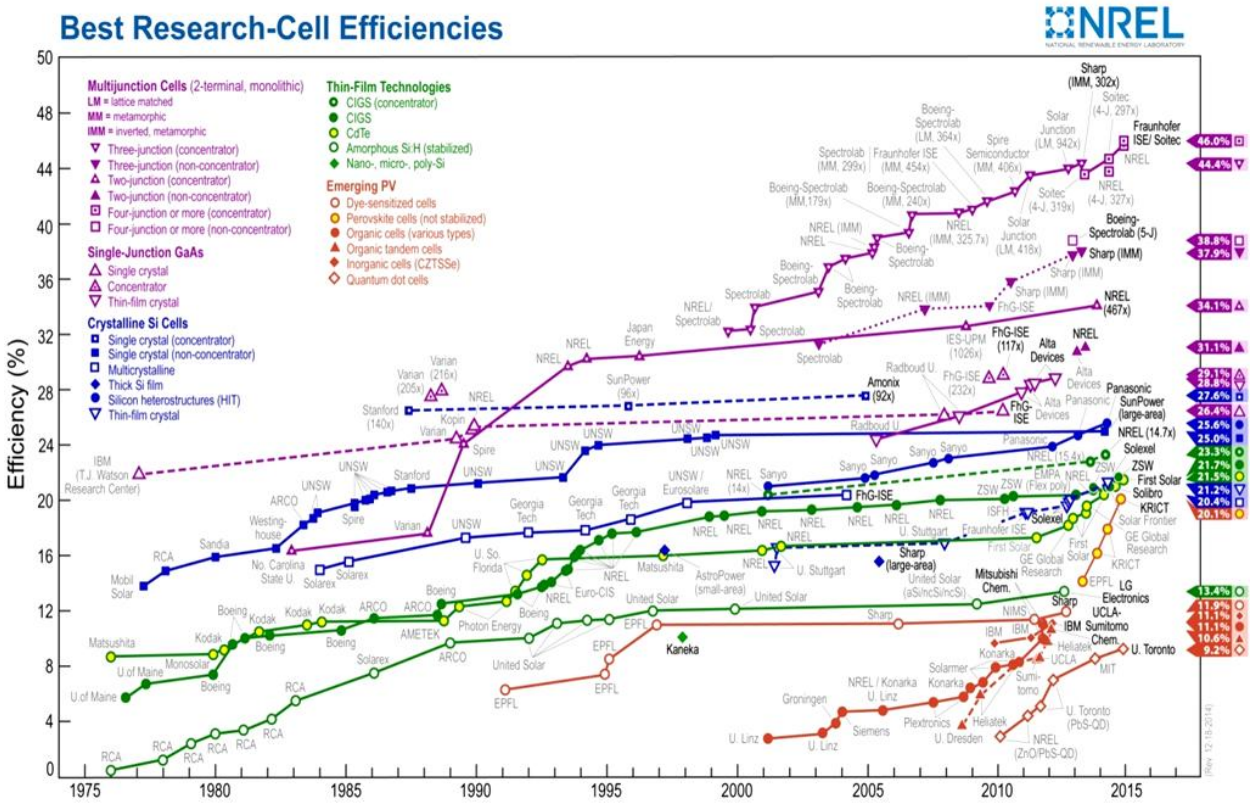

Figure 5: Best Research-Cell Efficiencies (This plot is courtesy of the National Renewable Energy Laboratory, Golden, CO) [15].

1-3-Physical basis of photovoltaics operation

The working principle of solar cells is based on the photovoltaic effect. In general, the photovoltaic effect means the generation of a potential difference at the junction of two different materials in response to radiation. The basic process lies on the generation of the charge carriers (electron and hole) due to absorption of photons in the materials that form a junction, followed by charge carriers separation and collection at terminals. Modeling and understanding of solar cell is very much simplified by using the pn junction (the diode) concept. This pn junction results from the "doping" that produces conduction-band or valence-band selective contacts with one becoming the n-side (lots of negative charge (electron)), the other the p-side (lots of positive charge (hole)).

The equivalent-circuit model for a PV cell is shown in Figure 6, as a light generated current source in parallel with a diode. The circuit includes photon generated current (I_{ph}), diode generated current [I_0(eqV/kT)], a series (r_s) and a shunt resistance (r_{sh}). According to the definition of the series and shunt resistance, the corresponding ideal values are 0Ω and ∞Ω, respectively.

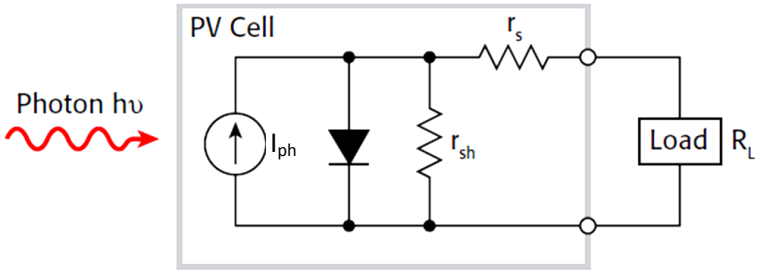

Figure 6: Equivalent-circuit model for a PV cell.

Current density [mA/cm^2] vs. Voltage [v] measurement is a simple method to evaluate photovoltaic device performance in dark or under illumination. A typical forward bias J-V curve of a PV cell is shown in Figure 7, and the most important parameters extracted from the curve will be explained briefly.

Measuring in the dark, J-V characteristics of a solar cell is similar to the exponential response of a diode with high current in forward bias and small current in reverse bias. Under illumination, the device generates a photocurrent in the cell in addition to the diode behavior, and the J-V characteristic under illumination is ideally the superposition of the dark characteristic of the diode and the generated photocurrent.

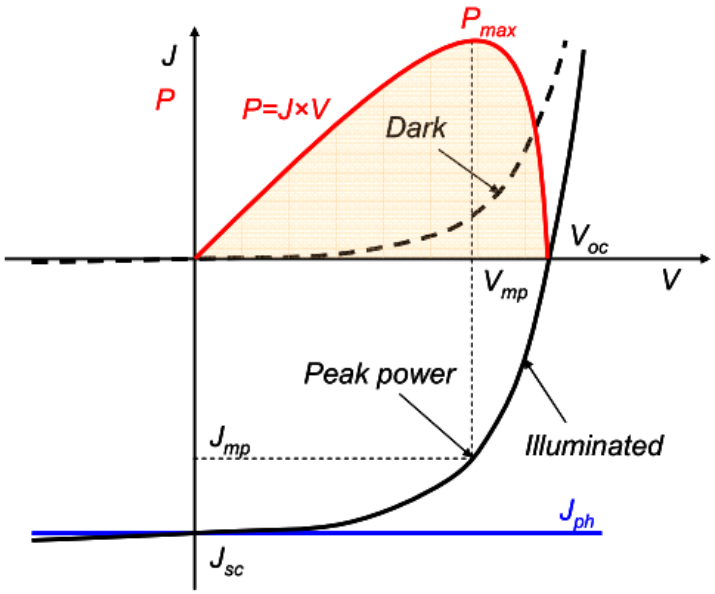

Figure 7: J-V characteristics of a p-n junction in the dark and under illumination.

The following Shockley diode equation under illumination describes the generated net current density:

$$J = J_0\left[\exp\left(\frac{qV_a}{kT}\right)-1\right]-J_{sc}$$

Where reverse saturation current density (J_0) is affected by recombination losses of the cell and Short-Circuit current density (J_{SC}) typically has a constant value.

Short-Circuit current density (J_{SC}): It can be read at the point where the voltage across the cell is equal to zero, and it is the maximum current that a device is able to produce. The number of photons (power of the incident light source)

also has an influence on the short circuit current, and hence the J-V measurement is done at the standard illumination at AM1.5, or 1000 W/m^2 which corresponds to 1 sun. The AM1.5 spectrum and its definition will be discussed in chapter 3-6.

Open-Circuit voltage (V_{OC}): It is the maximum voltage available across a photovoltaic cell, when no current is flowing. By setting the net current equal to zero in the solar cell equation, V_{OC} can be represented through the following equation:

$$V_{oc} = \frac{kT}{q} \ln\left(\frac{J_{sc}}{J_0} + 1 \right)$$

Fill Factor (FF): The fill factor is the ratio between the maximum power ($P_{max} = J_{mp} \times V_{mp}$) generated by a solar cell and the product of V_{OC} and J_{SC}. FF is a measure of the squareness of the J–V curve or how effective the solar cell performance is with respect to the ideal current generator (FF=1).

$$FF = \frac{J_{mp} V_{mp}}{J_{sc} V_{oc}}$$

The power conversion efficiency (PCE or η) is calculated as the ratio between the generated maximum power and the incident power. The irradiance value, P_{in}, of 1000 W/m^2 of AM1.5 spectrum has become a standard for measuring the conversion efficiency of solar cells.

$$\eta = \frac{P_{\max}}{P_{in}} = \frac{J_{mp} V_{mp}}{P_{in}} = \frac{J_{sc} V_{oc} FF}{P_{in}}$$

2-Perovskite based solar cells

Recent significant manufacturing costs reduction of silicon solar cell technology guarantees the future large-scale use of photovoltaics, anticipated to contribute nearly 30% of new electricity generation by 2030 [16]. As in microelectronics, silicon has a combination of advantages that has made it hard to be replaced as the favoured photovoltaic material. Opportunities exist for technologies that promise either significantly higher energy conversion efficiencies or significantly lower processing costs. A new generation of mixed organic–inorganic halide perovskites offers exciting prospects on both fronts [17].

Some key features of these PerovCells include ease of fabrication, strong solar absorption and low non-radiative carrier recombination rates for such simply prepared materials, in addition to the ability to capitalize on over 20 years of development of related dye-sensitized and organic photovoltaic cells. On the contrary, the negative aspect of perovskite is the fact that lead (pb) has been a major constituent of all highly performing PerovCells so far, raising toxicity issues during device fabrication, deployment and disposal. Also, they generally undergo degradation, sometimes quite rapid, upon exposing to the moisture and ultraviolet radiation [7].

Although the first efficient solid-state PerovCells were reported only in mid-2012, extremely rapid progress was made during 2013 and 2014 with energy conversion efficiencies reaching a confirmed 16.2% at the end of 2013 [7]. By November 2014, the most recent record certified nonstabilized efficiency of 20.1% was achieved by KRICT [15]. PerovCell concept is already ahead in the emerging PV efficiency race, having reached efficiency values that significantly surpass all of the ones obtained for other cells based on solution-processed materials and rapidly approaching existing commercial thin-film technologies [18].

On-going efficiency improvements are still predicted, as well as a fast growing understanding of their material properties and optimal cell designs. Moreover, a

broad range of different fabrication approaches and device concepts are represented among the highest performing devices; this diversity suggests that performance is still far from fully optimized and there are challenges facing the successful development and commercialization of such PerovCells.

2-1-Perovskite compound properties

A schematic illustration of the crystal structure of perovskite is shown in Figure 8b [4]. The general formula for hybrid perovskites is ABX_3, where A is methyl ammonium(CH_3NH_3), B is Pb(II) or Sn(II), and X is Cl, Br, or I, or a coexistence of several halogens. As an interesting material for solar cells, hybrid perovskites combine many advantageous properties. The most widely studied $CH_3NH_3PbI_3$ is a direct bandgap semiconductor with a bandgap of 1.55 eV determining its absorption offset up to 800 nm [19].

The weak photogenerated exciton binding energy of only 0.03 eV facilitates the charge separation at ambient temperature [20]. The lifetime of the carriers is also in the hundreds of nanoseconds' range, leading to much slower recombination and much longer diffusion length from 100 nm to 1000 nm [20]. Hole-transporting material-(HTM-) free PerovCells showed a PCE of 5.5% highlighting the unique efficient hole-transporting ability of $CH_3NH_3PbI_3$ [21]. Furthermore, long range ambipolar charge transport was found in $CH_3NH_3PbI_3$ [22]. All these material properties make perovskites exciting for photovoltaic applications.

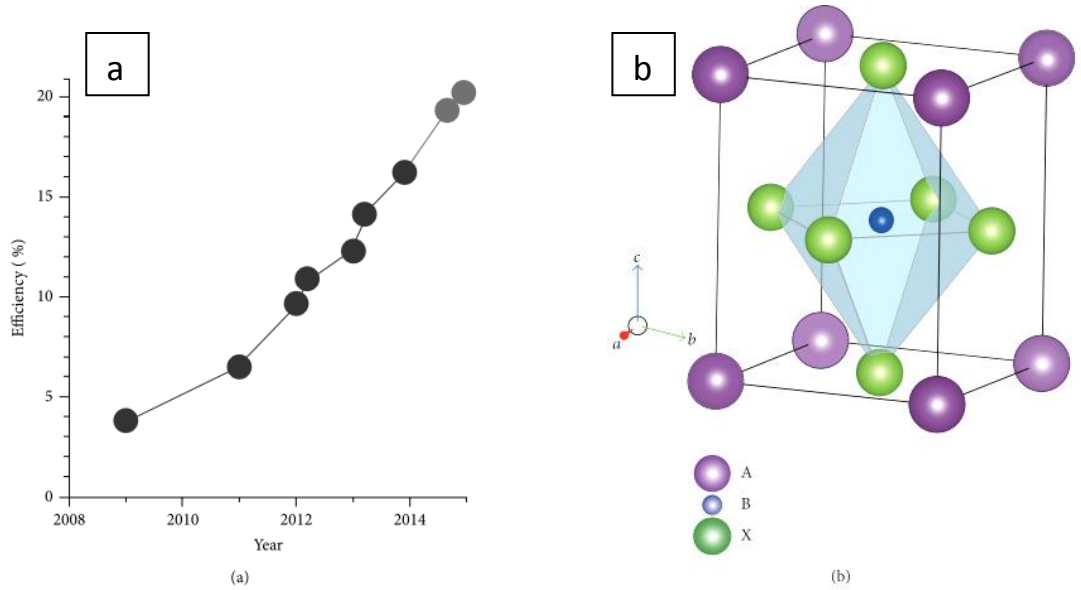

Figure 8: a) power conversion efficiency (PCE) record plot of PerovCells [15]. b) Crystal structure of perovskite adopting the form of ABX_3

2-2-Chronological developments

Miyasaka and co-workers [23] were the first ones to report photovoltaic results for perovskites; In 2006, they reported $CH_3NH_3PbBr_3$ cells with an efficiency of 2.2%; in 2009, by replacing bromine with iodine they managed to increase the efficiency up to 3.8% (although all devices were unstable) [24]. An organic liquid phase electrolyte containing lithium halide and the corresponding halogen formed the hole-transporting medium (HTM).

Park, Grätzel and colleagues [25] introduced a spiro-MeOTAD (2,2',7,7'-tetrakis(N,N-di-p-methoxyphenylamine)-9,9'-spirobifluorene) solid state HTM effective in solid-state dye cells. Spiro-MeOTAD not only improved the stability, as expected, it also boosted the reported efficiency to 9.7% [25]. The cell structure was encompassed by the

more general device of Figure 9 if the optional continuous perovskite layer is removed, leaving only scaffolding infiltrated by perovskite (and subsequently HTM).

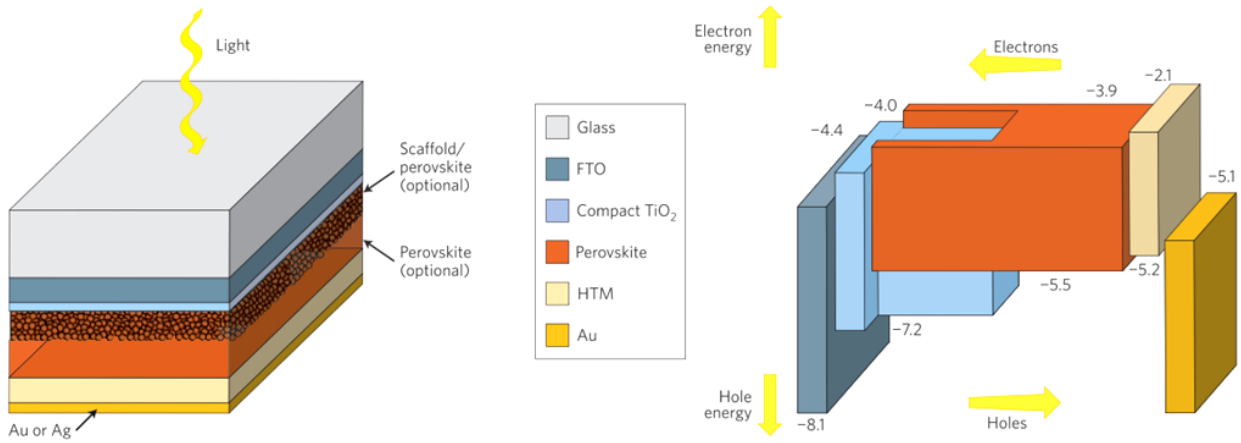

Figure 9: PerovCells structure and associated vacuum energy levels. General organic–inorganic halide solar cell, which includes two optional layers that are not essential for high performance [7].

By mid-2012, Snaith and co-workers [2] also reported success with spiro-MeOTAD in addition to four more developments that was crucial for PerovCell research field. The first development was the use of the mixed-halide $CH_3NH_3PbI_{3-x}Cl_x$, which exhibited better stability and carrier transport than its pure iodide equivalent. This type of perovskite was implemented in the current project. The second involved going beyond earlier nanoparticle structures by coating nanoporous TiO_2 surfaces with a thin perovskite layer and thereby forming extremely thin absorber (ETA) cells. The third was replacing conducting nanoporous TiO_2 by a similar but non-conducting Al_2O_3 network. This surprisingly improved the open-circuit voltage (Voc), boosting the reported efficiency to 10.9%; it also demonstrated that perovskites have a broader potential than just being used as sensitizers, as they are able to transport both electrons and holes between cell terminals. The fourth development exploited such

ambipolar transport by demonstrating simple planar cells with the scaffolding (Figure 9) completely eliminated.

A jump to a reported efficiency of 12.0% came from the combined efforts of Seok, Grätzel and colleagues using both optional layers (shown in Figure 9), including a solid perovskite capping layer overlying the scaffolding [22] (nanoporous TiO_2 infiltrated by perovskite). Both-optional-layer approach was implemented in the current project.

Further progress was reported at the European Materials Research Symposium in May 2013, with two groups reporting efficiencies above 15%. Grätzel's group used TiO_2 scaffolding and two-step iodide deposition, which improved the morphology [26].

Fabrication simplicity together with analogies with dye-sensitized and organic photovoltaics has resulted in a rapid increase in the number of researchers working in this field which is still in high increasing rate.

2-3-Photoanodes in Perovskite solar cells

2-3-1-Alumina and Titania photoanodes

Snaith and co-workers[2] exploited the extremely thin absorber (ETA) approach and used a perovskite absorber ($CH_3NH_3PbI_2Cl$) and mesoporous TiO_2 as the transparent n-type component, and spiro-OMeTAD as the transparent p-type hole conductor. These devices exhibited power conversion efficiencies near 8%, under simulated Air Mass (AM)1.5 full sun illumination.

The porous oxide films were fabricated from sol-gel processed sintered nanoparticles. The perovskite precursor solution was infiltrated into the porous oxide mesostructure via spin-coating, and was dried at 100˚C which enabled the perovskite to form via self-assembly of the constituent ions; dark coloration indicating perovskite formation was only observed after this drying step.

Interestingly, they also found that replacing the mesoporous n-type TiO_2 with insulating Al_2O_3 (illustrated in Figure 10) improved the power conversion efficiency toward 10.9%. Al_2O_3 is a wide band gap (7 to 9eV) insulator and purely acts as a "scaffold" upon which the perovskite is coated. They observed that electron transport through the perovskite layer itself (using Al_20_3 scaffold) is much faster than through n-type TiO_2. This "meso-superstructured solar cell" exhibited exceptionally few fundamental energy losses illustrated by generating open-circuit photovoltages of over 1.1 volts, despite the relatively narrow perovskite absorber band gap of 1.55 ev.

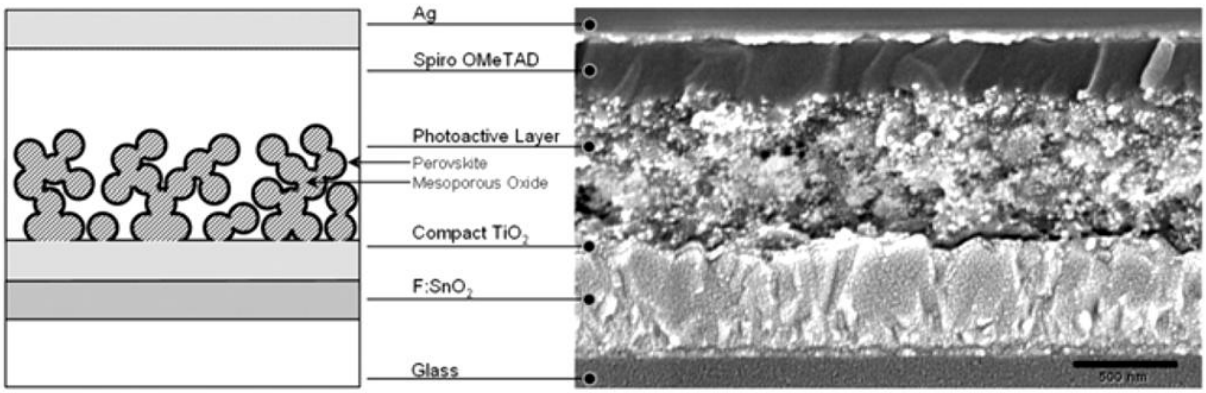

Figure 10: Schematic representation of full device structure, where the mesoporous oxide is either Al_2O_3 or anatase TiO_2 (left), Cross- sectional SEM image of a full device incorporating mesoporous Al_2O_3 (right).

In order to investigate the charge generation in these devices, they performed photoinduced absorption (PIA) spectroscopy on the oxide

films coated with the perovskite. For the mesoporous TiO_2 film coated with perovskite, the PIA spectrum revealed features in the near infrared assigned to the free electrons in the titania, confirming effective sensitization of the titania by the perovskite. In contrast, films made of Al_2O_3 coated with perovskite exhibited no PIA signal, confirming the insulating role of alumina. As represented schematically in Figure 11., the functionality arises from the use of mesoporous alumina as an inert scaffold which structures the absorber and forces electrons to reside in and be transported through the perovskite.

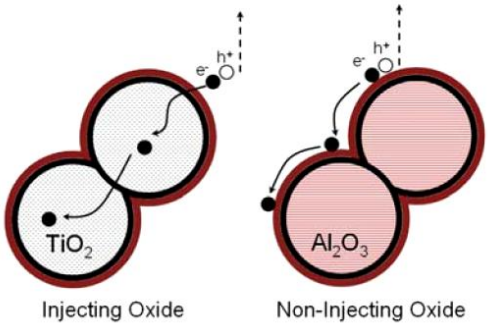

Figure 11: Scheme illustrating the charge transfer and transport in a perovskite sensitized TiO_2 solar cell, (left) and a non-injecting Al_2O_3 based perovskite solar cell, (right).

2-3-2-Zinc oxide photoanode

Organic–inorganic hybrid solar cells based on titania (or alumina) have emerged at the forefront of solution-processable photovoltaic devices; however, they require processing temperatures of up to 500˚C to sinter the mesoporous titania photoanode.

Liu and coworkers [3] reported the use of a thin compact film of ZnO nanoparticles as an electron-transport layer in $CH_3NH_3PbI_3$-based solar cells, shown schematically in Figure 12; in contrast to mesoporous TiO_2, the ZnO layer is both substantially thinner and requires no sintering suitable for flexible solar cells. ZnO is known to have an electron mobility that is substantially higher than that of TiO_2 [5]

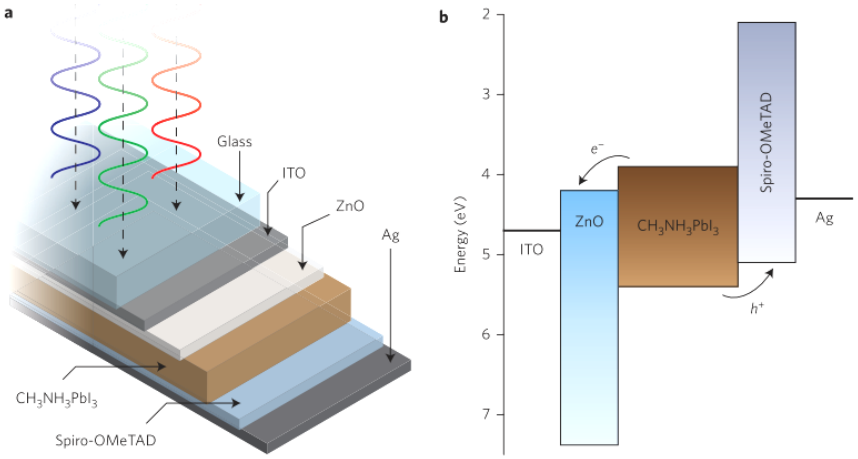

Figure 12: Device architecture and energy-level diagram. a) Device architecture of the ITO/ZnO/$CH_3NH_3PbI_3$/spiro-OMeTAD/Ag cell. b) Energy levels (relative to vacuum) of the various device components.

A two-step process was used to grow the $CH_3NH_3PbI_3$ layer [26] whose SEM image is shown in Figure 13. This consisted of spin coating a layer of PbI_2 onto the ZnO surface, followed by immersion of the substrate in a solution of CH_3NH_3. The efficiency of the subsequent devices was

found to vary with CH_3NH_3 concentration, solution temperature and dipping time, and care was taken to ensure that the processing conditions were reproduced as consistently as possible.

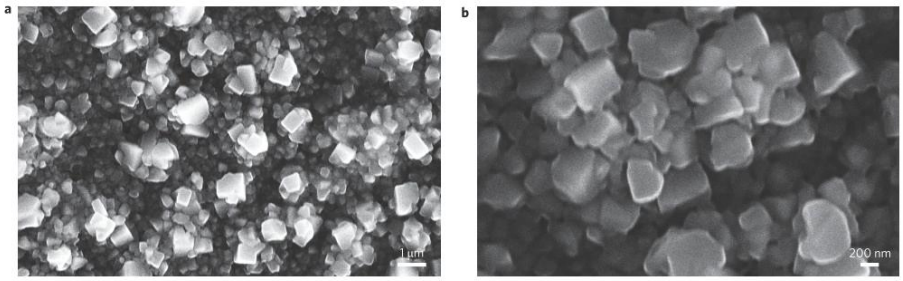

Figure 13: SEM micrographs of the ITO/ZnO/$CH_3NH_3PbI_3$ film. a) Low-magnification, b) High-magnification.

To study the effect of ZnO layer thickness on device performance, devices were prepared with ZnO of various thicknesses. As can be deducted from data in Table 1, the presence of an efficient electron-transport layer is crucial to obtain high-performance devices. Without the ZnO layer, the fill factor and open-circuit voltage (V_{oc}) are very low because of increased recombination at the ITO surface and a correspondingly low shunt resistance. Incorporating even a very thin (10 nm) ZnO layer into the device substantially improves both the V_{oc} and the fill factor, and for a ZnO thickness of 25 nm, power conversion efficiencies in excess of 14% were obtained.

Table 1: Device parameters for solar cells papered with varying thicknesses of ZnO.

No. of layers	ZnO thickness (nm)	J_{sc} (mA cm^{-2})	V_{oc} (V)	Fill factor (%)	PCE (%)
0	0	16.5	0.46	31.7	2.4
1	10	18.0	0.99	62.4	11.1
3	25	20.5	1.01	69.6	14.4
5	40	18.9	1.01	70.0	13.3
8	70	18.4	1.01	69.5	12.9

3-Techniques and experimental methods

3-1-Pulsed laser deposition

A general route used to synthesize thin films is through condensation of a vaporized form of the desired film material onto various workpiece surfaces. In particular, Physical Vapour Deposition (PVD) methods exploit physical processes for vapour formation from a target material such as thermal or electron beam heating and evaporation, sputtering by ions and, of course, ablation by photons. Among various deposition techniques, Pulsed Laser Deposition (PLD) is a PVD technique based on the production of plasma from a material target irradiated by intense laser pulses. PLD is believed to offer a great versatility for the production of a wide range of materials such as metals, ceramics, oxides, semiconductors, polymers and even biomolecules in the form of thin films and multilayers.

Among various materials, metals and metal oxides are established to be advantageous in a number of technological applications such as heterogeneous catalysis, photocatalysis, gas sensing, solar cells, biotechnology and medicine [27]. Performance of such materials closely relies on their structural and intrinsic properties. PLD enables the synthesis of nanostructured materials, in a bottom-up approach, with tailored physical and chemical properties through a fine tuning of the morphology and structure down to the nanoscale. This will pave the way for the design of materials with enhanced performances and/or novel properties.

In spite of the unique advantages of PLD, some shortcomings have been identified in using this deposition technique, such as splashing or the particulates formation. The physical mechanisms leading to splashing include the sub-surface boiling, expulsion of the liquid layer by shock wave recoil pressure and exfoliation. The size of particulates (droplets) may be as large as a few micrometers which will greatly affect the growth of the subsequent layers as well as the electrical properties of the films [28].

3-1-1-PLD Apparatus

The typical scheme of a PLD apparatus, as shown in Figure 14, is composed of a laser source and a vacuum chamber accommodating the target material and the substrate. Basically, laser pulses are focused on the target material inside the chamber through an optical path constituted by mirrors, lenses and a viewport. Laser pulses have a typical incidence angle of 40-50° with respect to the normal direction to the target surface while the substrate is placed in front of the target. The typical PLD systems, the one exploited in this project, consist in a stainless steel deposition chamber equipped with manipulators for the target (rotational and translational motion) and the substrate (x,y,z motion or z motion and rotation). Target manipulation is performed to optimize the position of the laser spot on the target in order to maintain a uniform ablation of the target surface. Substrate manipulation along the target-substrate axis is a fundamental parameter (the target-to substrate distance) while y, z motion and/or rotation around the z axis is exploited to deposit uniform films over wider areas (up to about 50x50 mm^2). A pumping system consisting of a primary and a turbomolecular pump and a gas inlet system with mass flow controllers and pressure gauges allows pressure control from 10^{-7} Pa to atmospheric pressure. A quartz crystal microbalance (QCM) can intercept the plasma plume to measure the deposition rate at different distances from the target.

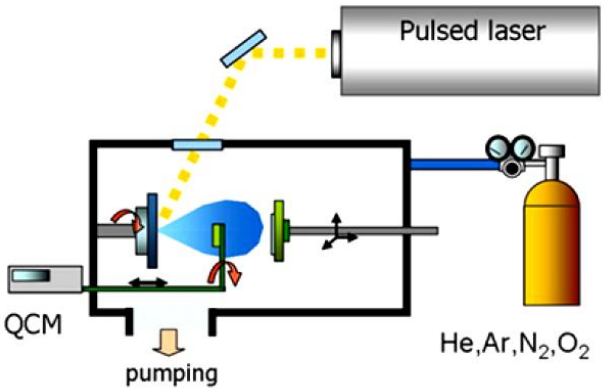

Figure 14: Scheme of the pulsed laser deposition apparatus

3-1-2-PLD mechanism and deposition of ablated species

The principle of pulsed laser deposition, in contrast to the simplicity of the system set-up, is a very complex physical phenomenon. It involves all the physical processes of laser-material interaction during the impact of the high-power pulsed radiation on a solid target. It also includes the formation of the plasma plume with high energetic species, the subsequent transfer of the ablated material through the plasma plume onto the substrate surface and the final film growth process. Thus, PLD generally can be divided into the following four stages:

i. Laser radiation interaction with the target
ii. Dynamic of the ablation materials
iii. Decomposition of the ablation materials onto the substrate
iv. Nucleation and growth of a thin film on the substrate surface

The formation of a plasma plume expanding in the normal direction from the target surface after laser-matter interaction is a key element of PLD. Usually in a PLD process, for laser pulses in the 5-15 ns range, the typical power transferred to the target is in the 10-100 MW range, corresponding to energy density (fluence) on the target of 1-10 J/cm^2. In such conditions the electric field in the material is in the order of 105 V/cm thus producing dielectric breakdown in any material which absorbs this energy [28]. When the fluence exceeds a threshold value (depending on the target material), the material is thus vaporized (ablated) forming the plasma.

Plasma plume expansion dynamics in vacuum is characterized by an almost collisionless propagation regime of the ablated species [29]. In such condition, the deposition regime is mainly characterized by high energetic (several tens of eV) atoms impinging the substrate. Atom-by-atom deposition of compact films is thus obtained (see Figure 15), in which the adhesion is improved by the high energy of the species impinging the substrate.

On the other hand, when an inert background gas is present in the deposition chamber the light emission increases due to collisions producing radiative de-

excitation of the ablated species, both in the body of the plume and particularly at the expansion front; the plume edge is better defined due to the presence of a travelling shock wave front which slows down until it reaches the so-called stopping distance [30]. The ablation plume is thus spatially confined and the presence of a background gas produces high pressure, temperature and density gradients at the shock front resulting in strongly out of equilibrium conditions [31]. The spatial confinement favours cluster nucleation in the gas phase. Clusters formed during the plume expansion dynamics may then diffuse in the background gas thus decreasing their kinetic energy. This condition may lead to low energy cluster deposition thus producing a cluster-assembled material in which clusters maintain, at least partially, their structure and properties.

Provided a reactive gas is used as a background atmosphere, as depicted in Figure 15, cluster composition may also be affected by the chemical interaction with the surrounding gas. This permits to deposit clusters with controlled composition. It opens the possibility to deposit metal oxide clusters by ablating a metallic target in the presence of oxygen.

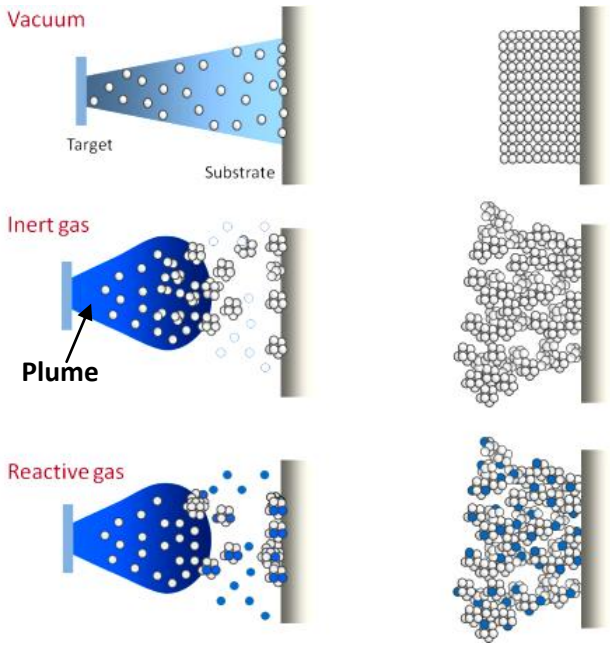

Figure 15: schematic view of the deposition process in vacuum and in the presence of inert and reactive gases

In the present work, ZnO was deposited by pulsed laser ablation of a solid ZnO (purity 99.99%) target by a ns-pulsed laser. The laser pulses (duration=6ns), interacting with the target, ablate its surface causing the formation of a “plume” of vaporized species which expands towards the substrate where the deposition takes place. All the depositions have been performed in the presence of oxygen as a background gas, introduced as pure O_2 in the chamber via a mks mass flow controller. The background O_2 pressure was varied from 10 to 400 Pa as discussed in the main text, with total deposition times ranging from 2 min to 20 min to adjust the relative thickness of the porous and compact layers. The typical flow rates were of the order of 250– 400 sccm for porous films (250 and 300 and 400 Pa O_2) and of 50 sccm for compact films (10 and 150 Pa O_2). Depositions were performed on (100) silicon, glass and Fluorine doped Tin Oxide (FTO) coated glass substrates. The laser fluence on the target was about 1 J cm^{-2} and the target to substrate distance was 50 mm.

3-2-Raman spectroscopy

Raman spectroscopy is one of the widely used techniques for material characterization. Raman scattering is employed to analyze the vibrational dynamics of the molecules or lattice cells constituting the material and it provides a sort of fingerprint of the analyzed material. It relies on inelastic scattering, or Raman scattering, of monochromatic light, usually from a laser in the visible or near ultraviolet range. Typically, a sample is illuminated with a laser beam; the laser light with frequency ω_L interacts with molecular vibrations, phonons or other excitations in the system, resulting in the energy of laser photons being shifted up or down, as schematically represented in Figure 16. The shift in energy gives information about the vibrational modes in the system. Light from the illuminated spot is collected with a lens and sent through a monochromator, it consists of a very strong line at the frequency ω_L , an also a series of much weaker lines with frequencies $\omega_L \pm \omega_j(q)$, where $\omega_j(q)$ are optical phonon frequencies. Wavelengths close to the laser line (ω_L) due to elastic Rayleigh scattering are filtered out while the rest of the collected light is dispersed onto a detector. The series of weak lines at $\omega_L \pm \omega_j(q)$ originates from inelastic scattering of photons by molecular vibrations or phonons, which constitutes the Raman spectrum. The Raman bands at frequencies $\omega_L - \omega_j(q)$ are known as Stokes lines, and bands at frequencies $\omega_L + \omega_j(q)$ are called anti-Stokes lines (see Figure 17). The intensities of the anti-Stokes lines are usually well weaker than those of the Stokes lines. In the first order of Raman scattering only optical phonons with $q \approx 0$ are involved, as a consequence of momentum conservation.

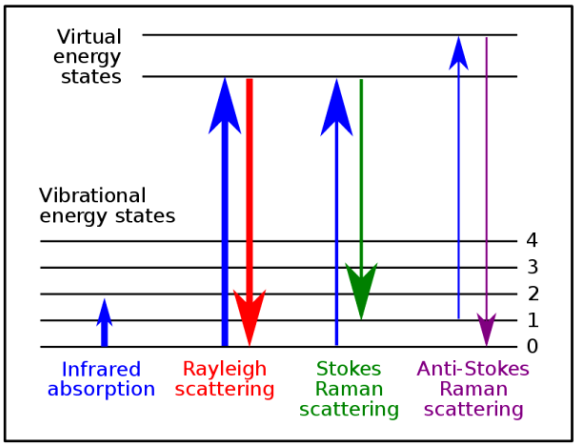

Figure 16: Energy level diagram showing the states involved in Raman signal. The line thickness is roughly proportional to the signal strength from the different transitions.

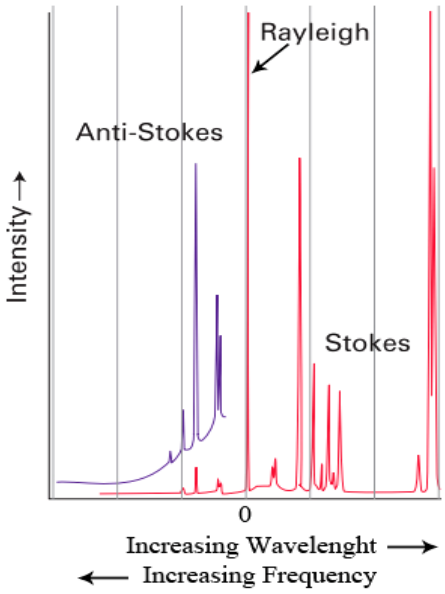

Figure 17: A typical Raman spectrum showing Rayleigh scattering (scattering of the laser light with no change in wavelength) and Stokes and anti-Stokes lines [32].

The following equation used to convert spectral wavelength to wavenumbers of shifts in Raman spectrum:

$$\Delta\omega\ (cm^{-1}) = \left(\frac{1}{\lambda_0(nm)} - \frac{1}{\lambda_1(nm)}\right) \times\ 10^7$$

where $\Delta\omega$ is the Raman shift expressed in wavenumber, λ_0 is the excitation wavelength, and λ_1 is the Raman spectrum wavelength. Usually, the units selected for expressing wavenumbers in Raman spectra is inverse centimeters (cm^{-1}).

The Raman instrument implemented in this work is the micro Raman system which is based on an optical microscope (Renishaw microscope, equipped with 5x, 20x, 50x and 100x short and long working distance microscope objectives) used to focus the excitation light and collect it in a back scattering configuration, a monochromator, notch filters system and a charge coupled detector. The sample is mounted on a translation stage of a Leica microscope. The excitation used consists of a diode laser at 532 nm. The system has been calibrated against the 520.5 cm^{-1} line of an internal silicon wafer. The spectra have been registered in the 40-500 cm^{-1} range. The final data have been averaged over five accumulations in order to maximize the signal to noise ratio. The measurements were conducted at room temperature and in air. The laser power intensity has been kept of the order of 300 μW in order to avoid any sample degradation effects.

3-2-1-Raman spectra of Perovskite

The significance of PerovCells was well discussed so far. Understanding the optical properties of perovskite film as the photon absorber material is essential for cell performance improvement. Perovskite consists of a MAX_3 structure, where MA, methylammonium, accommodates the organic cation $(CH_3NH_3)^+$ and X is the lead halide based on lead cation (Pb^{2+}) and iodine or chlorine (I^- , Cl^-) halide anions. The most developed perovskite materials for photovoltaics consist of methylammonium lead-iodide perovskite ($MAPbI_3$), along with its analogous mixed-halide perovskite ($MAPbI_{3-x}Cl_x$ or Cl-doped $MAPbI_3$).

In the previous study, Grancini et al. [33] have measured Raman spectra of $MAPbI_{3-x}Cl_x$ sensitized mesoporous alumina scaffold after annealing at 100°C for various durations, shown in Figure 18. In particular, they have identified three critical steps: (step 1) spin coating of the precursor solution without annealing treatment; (step 2) film annealed for 4 min at 100 °C; (step 3) film annealed for 45 min at 100°C.

The film fabricated up to the step 1 exhibits a Raman spectrum showing a main broad peak at around 104 cm^{-1}, related to the Pb−I modes [33]. The spectrum loses the characteristic Pb−Cl features (see $PbCl_2$ spectrum in Figure 18), in line with the predicted thermodynamic stability of the $MAPbI_3$ perovskite upon Cl to I substitution and suggests that, despite the use of $PbCl_2$ precursor, Pb−I bonds are quickly formed.

Upon 4 min annealing, the Raman spectrum dramatically changes; the spectrum indicates that this structure is an intermediate phase in the Cl-doped $MAPbI_3$ perovskite film formation.

Lastly, Raman spectrum of fully converted Cl-doped $MAPbI_3$ perovskite sample was attained (step 3). It was found that the longer annealing time in the presence of the $PbCl_2$ precursor allows for a reorganization of the organic−inorganic moieties within the crystal. The results indicated that the

chloride ions in the Cl-doped perovskite do not form a clearly detectable chemical bond with Iodine within the unit cell, neither any $PbCl_2$ residual is left over, but Cl has an important role in governing the crystallization process and the arrangement of the organic moieties.

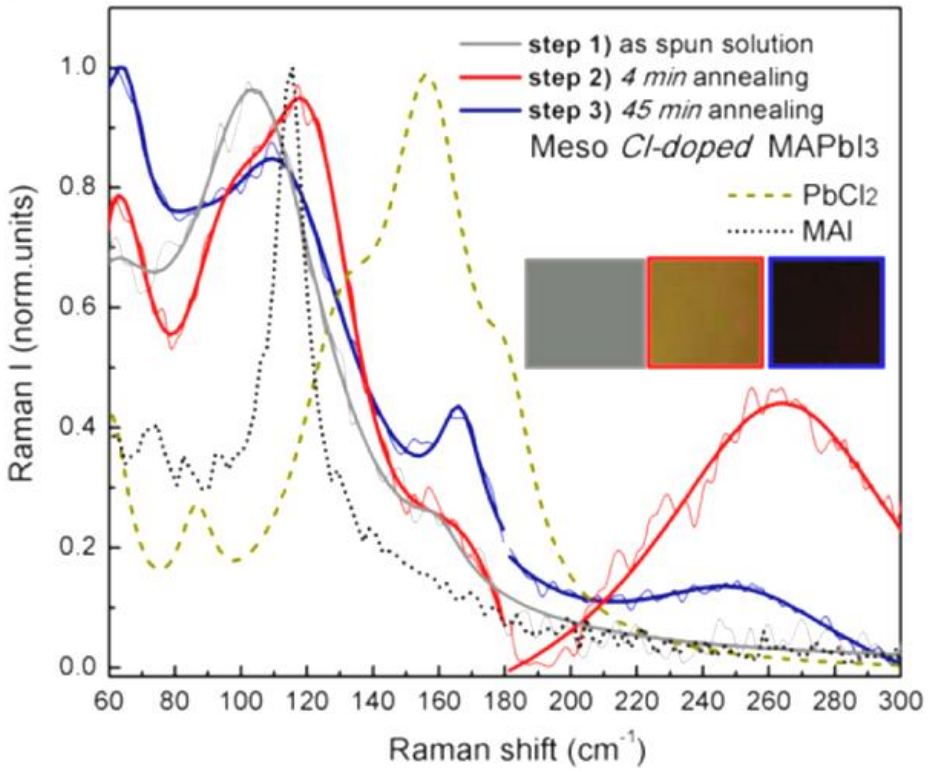

Figure 18: Raman Spectra of the perovskite solution precursor (dotted lines) and of the intermediate products (solid lies) during the Cl-doped $MAPbI_3$ film formation: (step 1) the "as spun" solution (gray line) as deposited on the substrate, (step 2) after 4 min annealing, and (step 3) the final perovskite film obtained at the end of 45 min annealing. Inset: cartoon of the film evolution at the three steps mentioned.

3-3-Scanning electron microscope

The scanning electron microscope (SEM) is one of the most versatile instruments available for the examination and analysis of the microstructure morphology and chemical composition characterizations. The unaided eye can discriminate objects corresponding to ~0.1mm resolution (at the optimum viewing distance of 25cm). Optical microscope has the limit resolution of ~2,000A˚. Scanning electron microscopy whose resolution can reach ~1nm has been developed by replacing the light source with high-energy electron beam.

Secondary electron signals produced as a result of electron/sample atoms interaction are detected displaying the topography of the surface. Specimens can be observed in high vacuum, in low vacuum, in dry conditions (in environmental SEM), and at a wide range of cryogenic or elevated temperatures.
In this work, SEM images of perovskite films have been collected using a high vacuum tungsten filament commercial Jeol 6010-LV scanning electron microscope, with a working bias of 5-6 kV. SEM images of ZnO films were acquired with a Zeiss SUPRA 40 field emission SEM. The samples were sticked on aluminium stubs with ultra smooth double-sided adhesive tape, made of conductive carbon.
A number of SEM images were quantitatively analyzed using Clemex professional image analysis software in order to determine film coverage and thickness in addition to crystallite size.

3-4-Ultraviolet–visible spectroscopy

Ultraviolet–visible spectroscopy is the observation of the absorption of electromagnetic radiation in the UV and visible regions of the spectrum [32]. It is among the most widely used techniques for studying inorganic compounds and their reactions.

The sample for a UV–visible spectrum determination is usually a solution but may also be a gas or a solid. Usually, the beam of incident radiation is split into two, one passing through the sample and the other passing through a cell that is identical except for the absence of the sample. The emerging beams are compared at the detector (a photodiode) and the absorption is obtained as a function of wavelength. Conventional spectrometers sweep the wavelength of the incident beam by changing the angle of a diffraction grating, but it is now more common for the entire spectrum to be recorded at once using a diode array detector (see Figure 19).

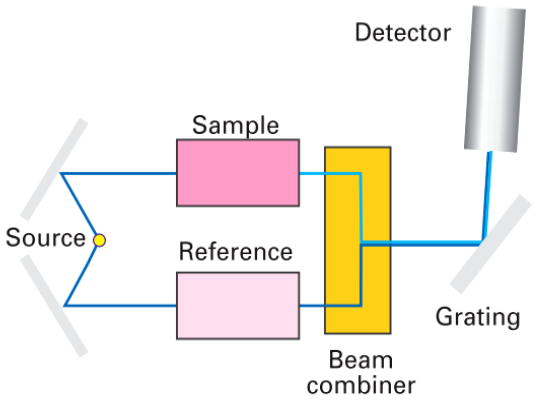

Figure 19: The layout of a typical UV–visible absorption spectrometer [32].

In the present work, absorption spectra have been attained by means of a UV-vis-NIR PerkinElmer 1050 spectrophotometer. The light source of the spectrophotometer is an alogen deuterium-tungsten lamp. They are the holographic grids with 1440 line/mm for ultraviolet and visible and 360

line/mm for infrared. The system has two different detectors, one for high energy and the other for the infrared spectral region. Moreover, an integrating sphere has been used due to high diffusivity of samples deposited at high PLD oxygen pressure; its role is to collect the transmitted radiation that has been scattered on all solid angle and not only the fraction that has not been deflected.

The Optical Density (OD) was evaluated according to the following equation:

$$I_T = (I_0 - I_R) \times 10^{-OD \times d}$$

where I_T, I_0 and I_R are the transmitted, impinging and reflected light respectively, and d refers to the sample thickness.

3-5-Spin coating

Spin coating is a procedure employed to deposit uniform thin films onto flat substrates. Parameters such as solution viscosity and concentration, spin velocity and dwell time can be optimized in order to achieve desirable thickness. The spin-coating process consists of four stages: deposition, spin up, spin off and evaporation. A typical process, schematically shown in Figure 20, involves depositing a small volume of a fluid material onto the centre of a substrate and then spinning the substrate at high speed. Centripetal acceleration will cause most of the fluid to spread to and off the edge of the substrate, leaving a thin film of material on the surface.

The main advantage of the spin-coating process is that it can produce highly uniform films over a wide range, provided planar substrates are used. Furthermore, the process can be tightly controlled in order to obtain reproducible film thicknesses [34]. For instance, by increasing the angular velocity or reducing the solution concentration the film thickness is reduced.

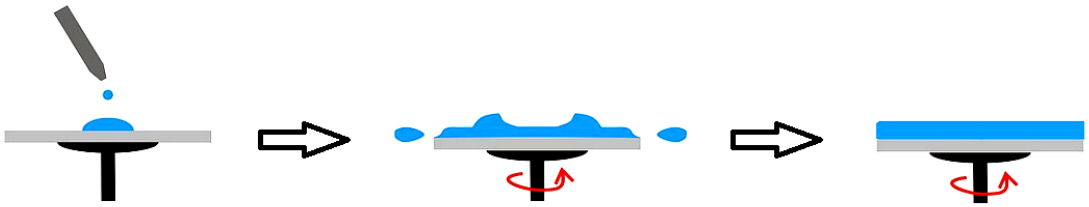

Figure 20: Simplified scheme of spin coating operation.

In the present work, to form the Cl-doped $MAPbI_3$ ($MAPbI_{3-x}Cl_x$) solution for subsequent spin coating, methylammonium iodide (MAI) and lead (II) chloride ($PbCl_2$) were dissolved in anhydrous N,N-Dimethylformamide at a 3:1 molar ratio of MAI to $PbCl_2$ with the final concentrations of 0.88M for $PbCl_2$ and 2.64M for MAI. The perovskite precursor was then spin-coated on the ZnO substrates in a nitrogen filled glovebox, at 2000 rpm for 60s, followed by an annealing treatment at 100 ˚C.

3-6-Solar simulator

A solar simulator is an instrument that provides illumination approximating natural sunlight. The purpose of the solar simulator is to provide a controllable indoor test facility under laboratory conditions, used mainly for the testing of solar cells [35]. A solar simulator consists of light source equipped with suitable filters required to modify the output beam to meet the classification requirements. Thus it is needed to select a light source that approximates the solar spectrum we aim to simulate, Air Mass 0 (AM0) for space applications and AM1.5 for terrestrial applications (see
Figure **21**). We also need to manipulate the beam via an optical system such that the spectrum and spatial uniformity of irradiance can be optimized for the required application.

Current density–voltage (J-V) curve is measured through solar simulator at standard illumination (AM1.5, 1 sun). 1 sun is typically defined as the nominal full sunlight illumination on a bright clear day on Earth, which measures 1000 W/m^2. Continuous light solar simulators may have several different lamp types combined (i.e. Xenon and multiple halogen lamps) to extend the spectrum far into the infrared.

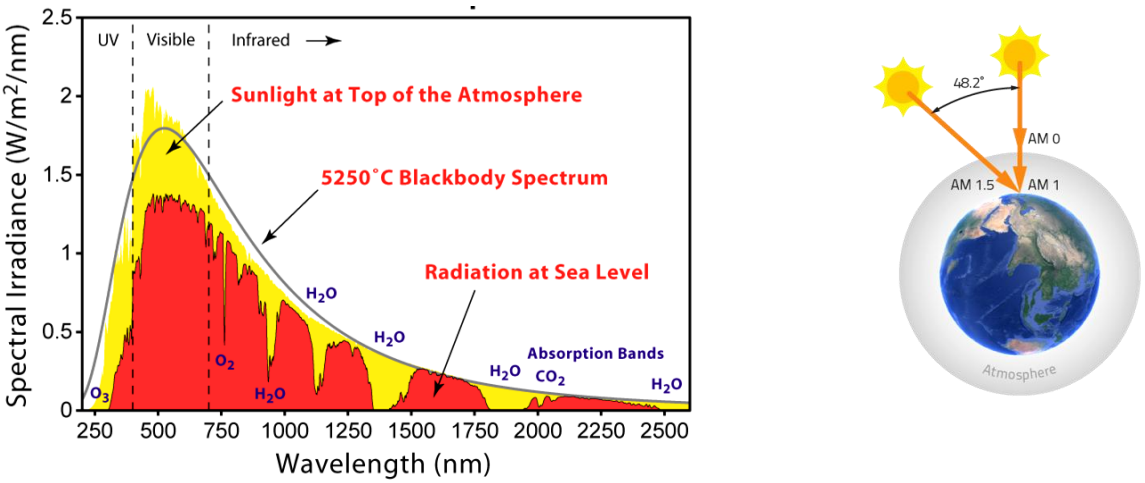

Figure 21: AM1.5 (Radiation at sea level) and Am0 (Sunlight at top of the atmosphere) sunlight spectrum with incidence angle of 48.2° [36].

In the present work, J-V characteristics were measured by a Keithley model 2400 digital source-meter exposing the cells to a class AAA Newport (AM 1.5) full spectrum. The power of incoming radiation was set at 1000 W/m^2 using a NREL calibrated silicon solar cell.

4-Result and discussion

The desirable perovskite photovoltaic architecture we aim to realize is represented schematically in Figure 22. Materials for device stack of layers were selected based on suitable energy levels for ideally highest performing device [7].

Favorable photoanode structure in the PerovCell of interest is a double layer structure. Double layer structure refers to a ~200nm-thick hierarchical ZnO film on top of ~60nm-thick compact layer ZnO. Compact ZnO layer will act as the hole blocking layer between perovskite and FTO. Without this blocking layer, fill factor and open-circuit voltage decrease due to increased recombination at FTO surface resulting in correspondingly weak cell performance with low shunt resistance [3]. Hierarchical photoanode is also well established to increase electron lifetime (so better charge collection efficiency), in comparison to the benchmark mesoporous films, probably due to lower surface defect density or to good interparticle connection [8]. Furthermore, hierarchical architecture combines the efficient light harvesting and increased surface area for dye (here perovskite) absorption, all beneficial for cell operation [9].

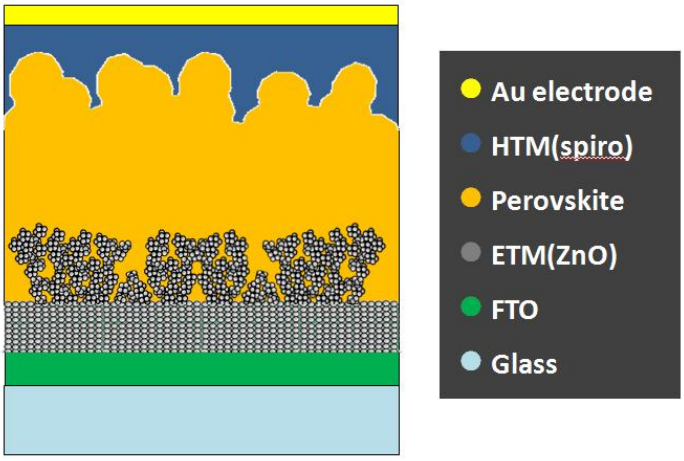

Figure 22: schematic image of favorable device architecture.

Understanding how PLD parameters including PLD oxygen chamber and PLD duration influence ZnO film characteristics is of fundamental importance to control the fabrication of favorable photoanode structure. Chamber oxygen pressure will determine ZnO film degree of porosity [37] and PLD duration is proportional to ZnO film thickness, in principle. However, PLD process fine optimization is required to determine how to achieve accurately favorable thickness and compactness/porosity as will be discussed thoroughly in chapters 4-1-1 and 4-1-2.

The next step, addressed in chapter 4-2-1 and 4-2-2, was aimed to probe how ZnO photoanode characteristics in terms of thickness and porosity influence perovskite film absorber ($CH_3NH_3PbI_{3-x}Cl_x$) in terms of perovskite crystallite size, morphology and film coverage. We also studied how annealing time can affect perovskite sensitized ZnO film in order to obtain desirable annealing time range (chapter 4-3).

The last step was to fabricate the final device architecture according to optimized conditions. Devices were made adopting double layer ZnO structure with two different porous layer thicknesses (chapter 4-4-1). Photoluminescence and optical density of perovskite sensitized ZnO films were obtained to investigate the possible effects of annealing duration and ZnO film thickness on optical properties (chapter 4-4-2-1). Finally in chapter 4-4-3, HTM and gold electrodes were deposited on perovskite sensitized ZnO films to achieve the ultimate device architecture. J-V curves were subsequently measured by means of solar simulator and we tried to relate cell operation to the fundamental properties of the constituent materials. All figures presented in chapter 4 (result and discussion) refer to the current project's results.

4-1-Effect of PLD parameters on ZnO film characteristics

4-1-1-Chamber oxygen pressure/ZnO film porosity dependence

The ZnO film presented in this work were grown by PLD at room temperature on different type of substrates including silicon, glass and FTO. Laser pulses in the nanosecond regime were focused on the ZnO (purity 99.99%) target. Energy density in the 0.90 J/cm^2 range was chosen to maximize deposition rates while minimizing droplet ejection from the target as much as possible. Oxygen background gas was used with typical pressure in the 10-400 Pa range with total deposition times ranging from 2 min to 20 min. Target-to-substrate distance (d_{TS}) was chosen to be 50mm.

The first run PLD was carried out at different chamber oxygen pressures, namely 10, 150, 300 and 400Pa whose SEM images are shown in Figure 23a-d, respectively. The first run was aimed to find out suitable oxygen pressure to fabricate the solar cell oriented double layer structure (composed of porous ZnO film grown on top of compact ZnO film)

The oxygen pressure increase was associated with increasing ZnO film porosity and ZnO droplet frequency, as can be observed in Figure 23a-d.

Basically, at 10 and 150Pa cases, the films seem compact and droplets can hardly be found on the film surface (top view as inset images). The white dots observed in Figure 23a and b (top view images) indicate the tip of directional clusters and must not be confused with droplets.

Higher deposition oxygen pressure (300Pa) induces clustering phenomena in the ablation plume, which results in formation of nanoporous semi-hierarchical assemblies of nanosized clusters (cross-section view). This nanoporous morphology is the favorable photoanode structure we aimed to fabricate. On the film deposited at 300Pa, appreciable number of droplets can also be observed (top view).

The void and porosity volume fraction of film deposited at 400Pa are so much that an inhomogeneous open structure was formed which is far from the

favorable hierarchical structure. Plus, the film contains so many droplets with various sizes. In general, PLD-grown films often exhibit micrometre-size droplets whose density and size distributions depend on laser wavelength, laser fluence, pulse width and ambient gas pressure [38]. In order to understand the mechanism of droplet formation, a number of approaches have been addressed in previous studies.

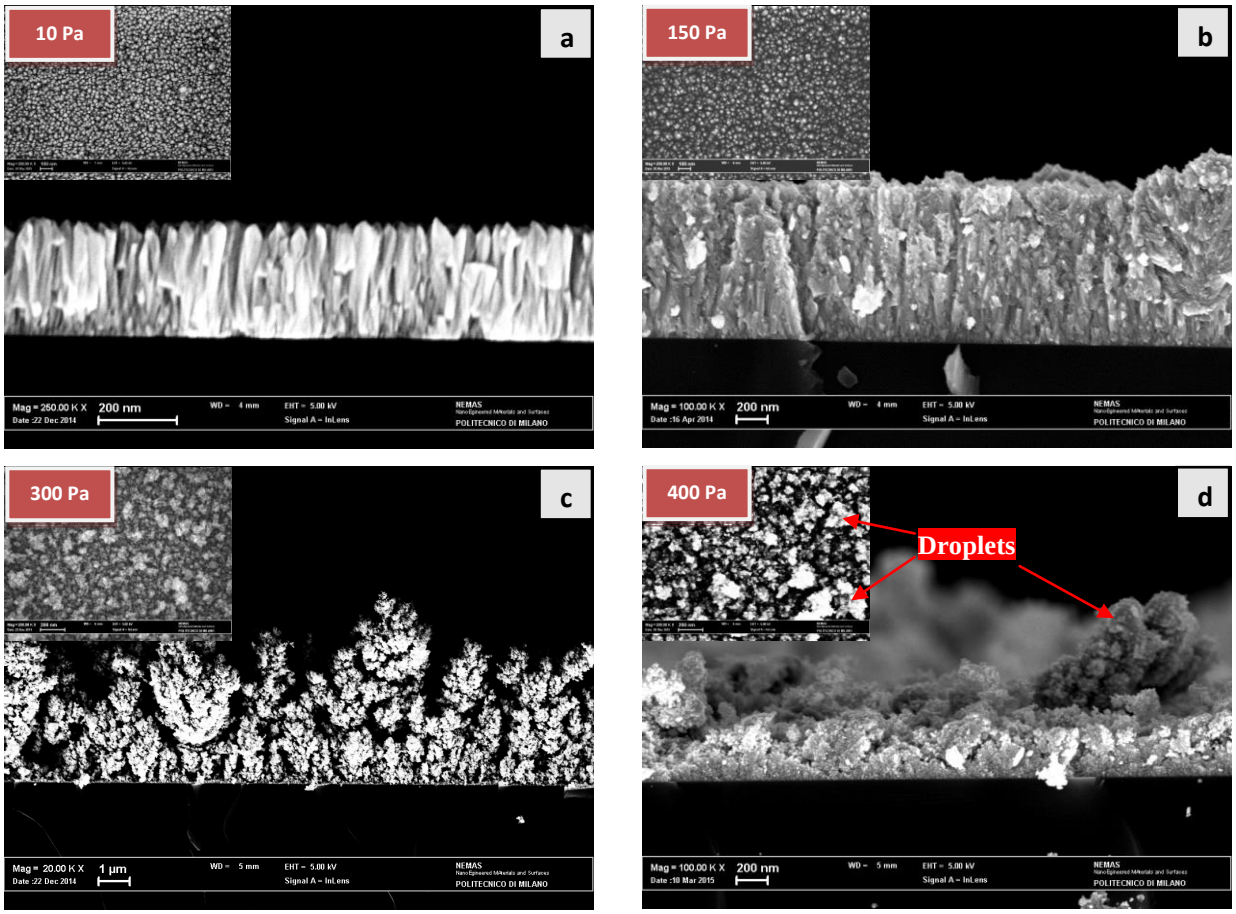

Figure 23: SEM images of ZnO films deposited by PLD in oxygen background gas at different pressures a) 10 Pa; b) 150 Pa; c) 300 Pa and d) 400 Pa.

4-1-2-PLD duration/ZnO film thickness dependence

PLD was carried out at different chamber oxygen pressures for various durations. Figure 24 summarizes ZnO film thicknesses obtained after PLD depositions at 10, 250 and 300Pa for various durations ranging from 2 to 20min.

It is common sense that, at a given oxygen pressure, increasing PLD duration results in film thickness increase in a linear way, in principle.

However, this linearity (represented by fitting line passing from practical measured thicknesses) was found to be respected rigorously at the lowest pressure case (10Pa), indicated by R^2 =1. At high pressure case (300Pa), measured thicknesses for various durations follows the linearity with slight deviation, indicated by R^2 =0.9775. Since PLD was done only at a single duration at 250Pa, R^2 value cannot be reported for the fitting line.

Additionally, at a given duration, ZnO film thickness increases by increasing the oxygen pressure. In other words, at a given duration, by increasing the oxygen pressure, the amount (the mass) of ZnO film deposited on the substrate is constant while the density of film decreases (lower compactness) due to increased volume fraction of pores. The lower density gives rise to higher total volume occupied by film which in turn results in higher thickness. The latter is indicated by higher fitting line slope at higher pressure cases.

What's more, ZnO film deposited at high oxygen pressure (300Pa) contains considerable number of droplets; In fact, droplets contribute significantly to the final film structure as schematically represented in Figure 25. Therefore, droplets' average thickness was also determined and reported, indicated by positive error bars in Figure 24. Droplets are not present at compact films (10Pa) nor does the error bar. 400Pa structure was so inhomogeneous that finding the reasonable average film and droplets' thickness was irrelevant.

According to our findings, in order to fabricate desired double layer structure, 10Pa was chosen for compact film and 300Pa was selected to make the

nanoporous structure. Favorable thickness for double layer structure can be also derived from thickness/PLD duration fitting line of relevant pressures, Thickness(nm)=14.698×Time(min) for 10Pa and Thickness(nm) =34.341×Time(min) for 300Pa.

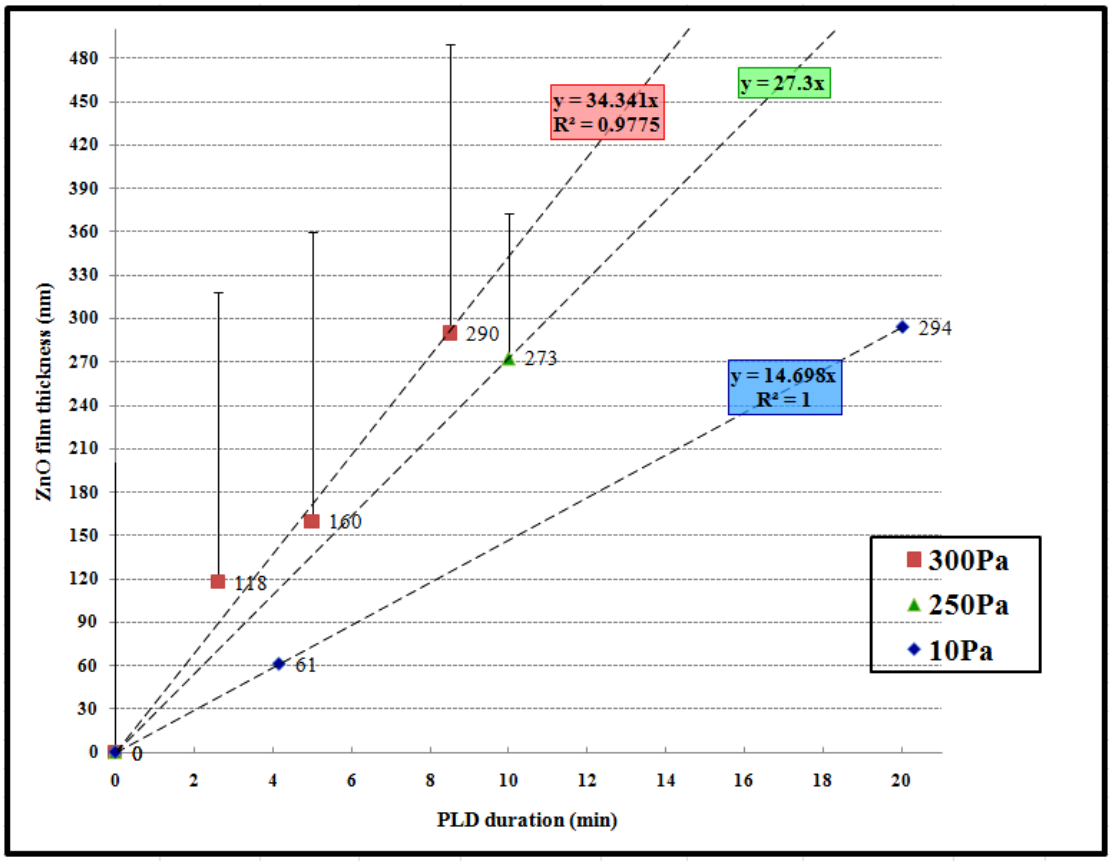

Figure 24: PLD duration/ film thickness dependence for ZnO film deposited at various oxygen background gas pressures.

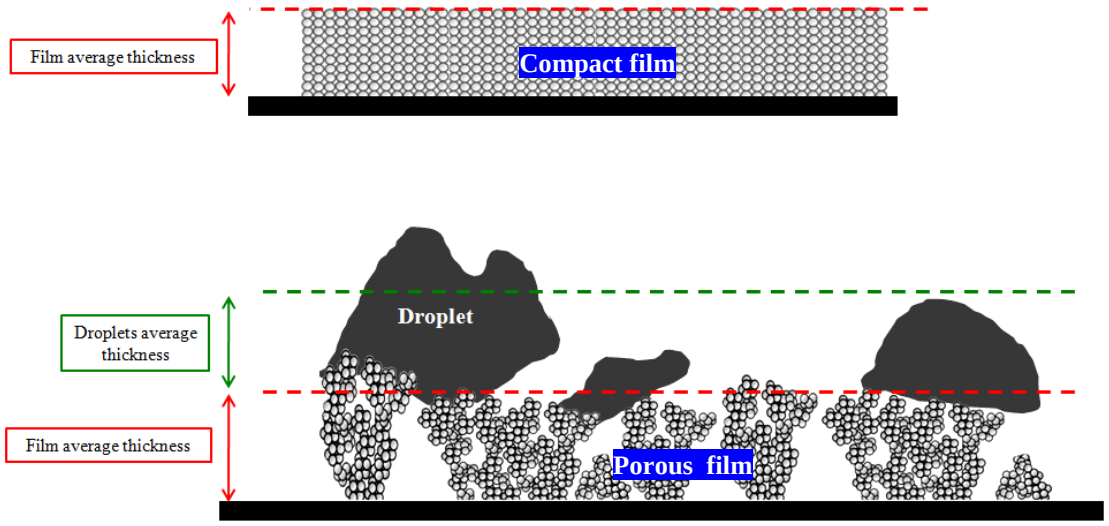

Figure 25: Schematic illustration of how film and droplets' average thicknesses were calculated.

4-2-Effect of ZnO photoanode characteristics on perovskite structure

The substrates made by PLD include ZnO films with various thicknesses and porosities. To analyze the effect of possible moisture entrapped within ZnO film pores, after PLD and before perovskite spin coating, a number of samples were pre-heated in a nitrogen filled glovebox at 120˚C for 45min (hereafter referred to as H1) so as to evaporate the moisture; some other samples remained without pre-heating (hereafter referred to as H0).

To form the perovskite layer, the perovskite precursor was spin-coated on the ZnO substrates in a nitrogen filled glovebox, at 2000 rpm for 60s. Then, they were immediately annealed on a hotplate in the glovebox at 100˚C for different durations namely 10, 30 and 60s in order to achieve the standard perovskite chemical composition. The temperature of 100˚C was already proposed to be the optimized temperature to form pervoskite layer with the highest absorption on compact TiO_2 substrates [39].

Different combinations of ZnO film thickness and porosity in addition to multiple perovskite annealing time were examined to analyze each parameter's contribution to the perovskite structure. To better distinguish different set of conditions, a few notations were used throughout the context whose definitions are presented in Figure 26.

Figure 26: The notations used to distinguish different set of conditions.

300Pa (or 400Pa) refers to PLD chamber oxygen pressure. It is an indication for ZnO film porosity.

10min (or 5min) refers to the PLD duration. It is an indication for ZnO film thickness.

H1 indicates that ZnO film was pre-heated at 120˚C for 45min prior to perovskite spin coating. **H0**, on the contrary, implies no pre-heating.

10s (or 30s or 60s) refers to annealing time always at 100˚C immediately after perovskite spin coating.

■ The square's color roughly approximates the actual sample's color once the perovskite annealing is completed. The colors can be black, gray or white.

It is noteworthy to discuss some general microstructure features of perovskite SEM images. Figure 27-a shows the top view SEM image of 10s annealed perovskite sensitized ZnO film (fabricated at 300Pa chamber oxygen pressure for 5 minutes by PLD) at 100˚C. The spherical islands, seen at Figure 27-a, are believed to be perovskite crystallites according to obtained Raman spectra (Figure 27-b) of the same sample and absorption spectra (discussed later in chapter 4-4-2-1-2). The peaks of Raman spectra (Figure 27-b) for our sample (Glass/ZnO/$CH_3NH_3PbI_{3-x}Cl_x$) almost consistently resembles that of perovskite ($CH_3NH_3PbI_{3-x}Cl_x$) sensitized alumina mesoporous scaffold reported in literature [33].

Briefly, the peak at lower frequencies, around 62 cm^{-1}, represents the diagnostic modes of the inorganic cage. The peak at around 111 cm^{-1} is associated with the organic libration modes along with the unstructured feature in the frequency range of 150 − 160 cm^{-1}. Moreover, the broad, intense band at about 258 cm^{-1} is assigned to the organic torsional mode [33].

The same study also suggests that the presence of chloride ions in the starting composition does not change the chemical nature of the inorganic cage, but it affects the local structure, inducing a preferential order of the organic cation $(CH_3NH_3)^+$ organization in the inorganic cage.

The sample's black coloration can be another indication of perovskite formation. The band gap of $CH_3NH_3PbI_{3-x}Cl_x$ perovskite is about 1.6ev (~770nm) [33] that means most of the visible spectrum, ~380nm-750nm, can be absorbed by perovskite layer resulting in the sample's black color. High visible range absorption positively affects solar cell performance. Accordingly, our findings confirm that perovskite requires surprisingly short annealing time at 100˚C, less

than one minute and about 10 seconds, when spin coated on PLD-fabricated ZnO film. 1-minute annealing time at 100˚C was already reported to be favorable for the case of nanoparticle-fabricated ZnO substrate [6].

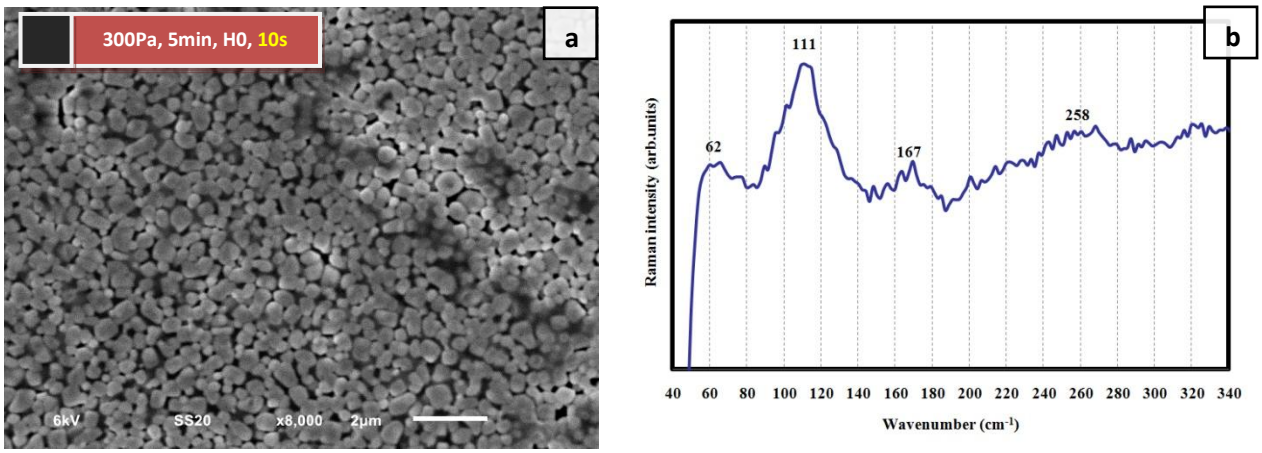

Figure 27: a) Top view SEM image of 10s annealed perovskite sensitized ZnO film (fabricated at 300Pa chamber oxygen pressure for 5 minutes); b) Raman spectra of Glass/ZnO/$CH_3NH_3PbI_{3-x}Cl_x$ substrate.

4-2-1-Effect of ZnO film thickness

In general, there are three features which can be discussed looking at the perovskite SEM images, crystallites size, crystallites morphology and perovskite film coverage (ie. how completely perovskite layer covers ZnO substrate).

To begin with, PLD duration (ie. ZnO film thickness) was chosen as the variable, while other parameters remained unchanged. Figure 28a and b show the top view SEM images of 10s annealed perovskite sensitized ZnO film fabricated at 300Pa chamber oxygen pressure for 5 and 10 minutes by PLD. As can be observed in Figure 28-a and b, ZnO film thickness alteration does not change the crystallites diameter size whose value is 400±20nm in both cases.

Our observations suggest that the coverage is also not affected by ZnO film thickness. The degree of coverage in this case is 84% which is an important factor to achieve high performing cell according to previous study [39]. The same study [39] also suggests that increasing the thickness of compact TiO_2 photoanode from 75nm to 225nm was associated with perovskite coverage improvement from 90% to 98%, respectively. It was speculated that n-type TiO_2 compact layer may interact electronically with the perovskite film during formation; possibly a thicker layer is able to transfer more electronic charge to the perovskite assisting its formation near the surface due to differing electrostatics. However, change in the coverage by changing the porous ZnO film thickness was not found to be the case in the current work.

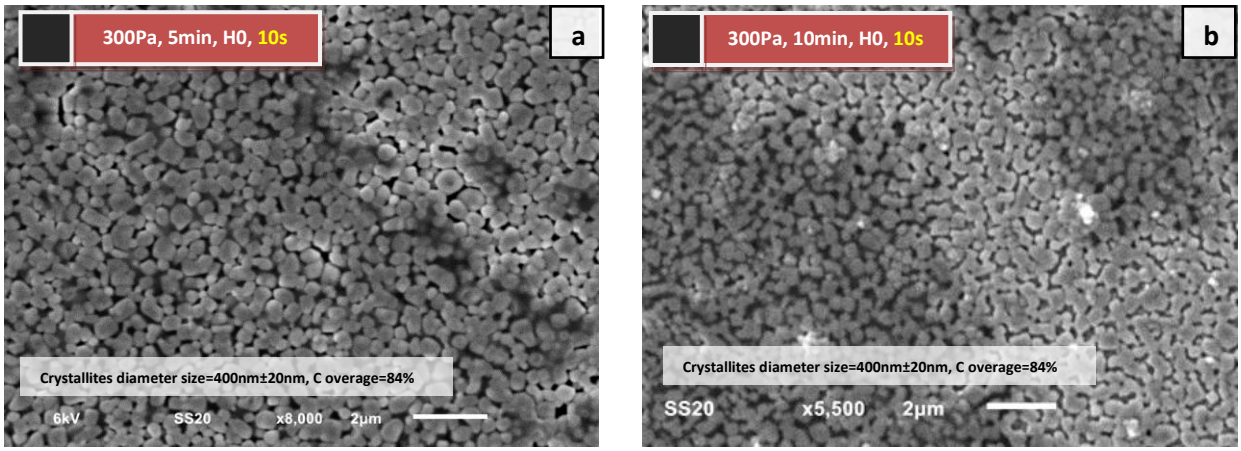

Figure 28: Top view SEM images of 10s annealed perovskite sensitized ZnO film fabricated at 300Pa chamber oxygen pressure for a) 5 and b) 10 minutes by PLD.

4-2-2-Effect of ZnO film porosity

Next step was taken to examine the effect of ZnO film porosity on the perovskite microstructure keeping other parameters unchanged. ZnO film fabricated at 400Pa chamber oxygen pressure showed higher degree of void and porosity compared to that of 300Pa. Figure 29a and b show top view SEM images of 10s annealed perovskite sensitized ZnO film fabricated at 400Pa chamber oxygen pressure for 5 and 10 minutes by PLD. Similar to 300Pa case, thickness of ZnO film fabricated at 400Pa does not contribute to any variation in perovskite crystallites size, crystallites morphology and coverage. The samples' color also look black implying high visible range absorption associated with perovskite formation. As can be seen, perovskite crystallites diameter size is about 60nm smaller in the case of 400Pa with respect to 300Pa. De Bastiani et al. [6] have already shown that the perovskite morphology is substantially affected by nanoparticle diameter size (20, 50 and 70nm) in nanoparticle-fabricated ZnO substrate keeping the ZnO film thickness constant (800nm).

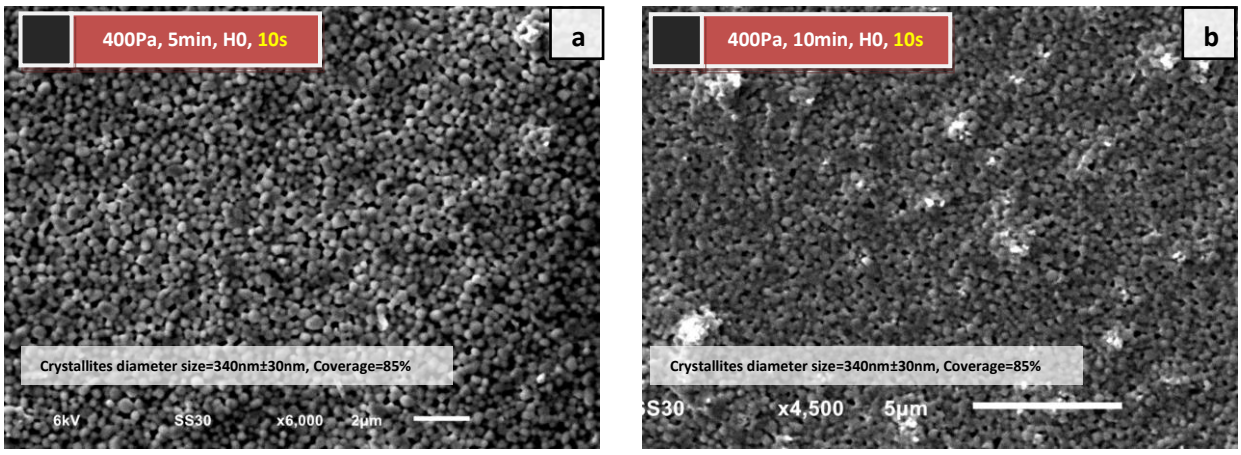

Figure 29: Top view SEM images of 10s annealed perovskite sensitized ZnO film fabricated at 400Pa chamber oxygen pressure for a) 5 and b) 10 minutes by PLD.

4-3-Effect of annealing time on perovskite structure

The annealing time of about 10seconds for perovskite sensitized ZnO film at 100˚C was mentioned to be sufficient to form standard perovskite composition according to Raman spectra. However, we attempted to study longer annealing times (30s and 60s) in order to attain complete understanding of possible phase transitions. In this regard, two identical ZnO substrates being fabricated at 400Pa chamber oxygen pressure for 10 minutes were selected. They were sensitized by perovskite and annealed immediately at 100˚C for 10 and 60s. In spite of only 50s difference in annealing duration, perovskite microstructure and samples' color look totally different (see Figure 30a and b). By increasing the annealing duration from 10s to 60s, sample's color has shifted from almost black to almost white suggesting degradation in the absorption in visible spectrum. Besides, morphology has been completely changed from spherical perovskite crystallites (340±30nm) to bigger islands surrounded by rod-like crystallites (~2000±400nm). Literature [40] and our photoluminescence measurements (discussed in chapter 4-4-2-1-1) ascribe these rod-like crystallites (pointed by yellow arrows) to PbI_2 formed as a result of over annealing condition. In previous study [40], it was shown that $CH_3NH_3PbI_3$ decomposes upon heating at 150˚C for prolonged annealing time, where CH_3NH_3I species escaped from the perovskite film to form the PbI_2 phase. "Annealing too long will degrade the perovskite film, which deteriorates the device performance by introducing a large amount of excessive PbI_2" [40].

In a nutshell, over annealing is associated with PbI_2 formation (lower photoluminescence intensity, chapter 4-4-2-1-1), sample's color shift toward gray (degradation in visible light absorption, chapter 4-4-2-1-2) and correspondingly expected poor solar cell performance.

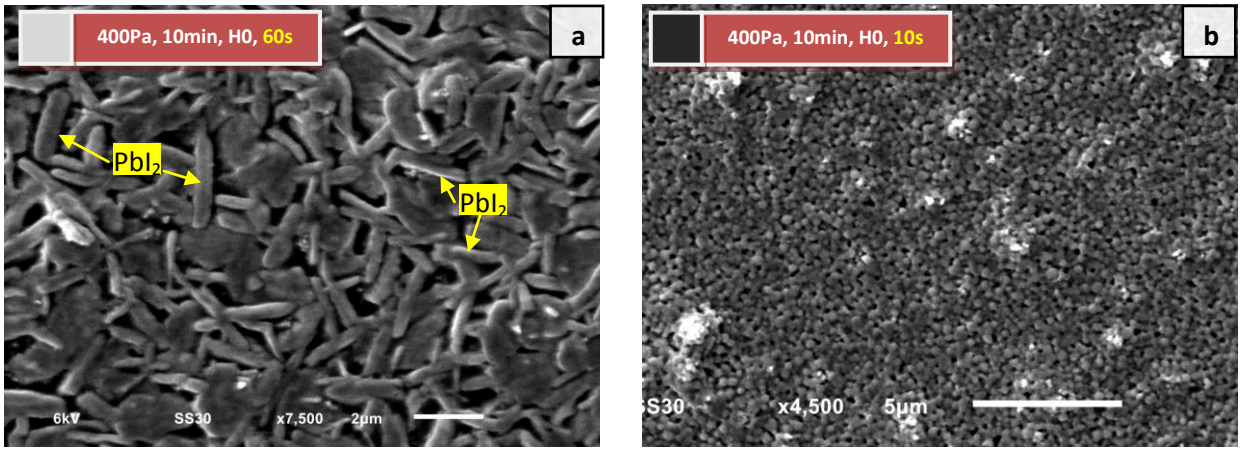

Figure 30: Top view SEM images of perovskite after annealing at 100˚C for a) 60s and b) 10s on top of ZnO film (fabricated at 400Pa chamber oxygen pressure for 10 minutes by PLD).

In order to better trace the transition between sphere crystallites (perovskite) to rod-like crystallites (PbI_2), 10 and 30s annealing duration were chosen. The latter was carried out in two different conditions; first, two ZnO substrates (PLD fabricated at 300Pa for 10 minutes) were directly used for perovskite spin coating without any pre-heating. This was also the case for all samples studied so far which are indicated by notation H0. Second, two other ZnO substrates (PLD fabricated at 300Pa for 10 minutes) were pre-heated in a nitrogen filled glovebox at 120˚C for 45min and then cooled down to ambient temperature. They were subsequently spin coated by perovskite. The second condition is indicated by notation H1.

Figure 31a shows the presence of pbI_2 rod-like crystallites (indicated by yellow arrows) after only 30s annealing for non-preheated ZnO film. As we observed in Figure 30a, the volume fraction of PbI_2 increases dramatically by increasing the annealing duration. Figure 31a indicates that the sample color is also shifted toward gray in presence of PbI_2. On the other hand, no PbI_2 is detected after 30s annealing for preheated ZnO film suggesting a delay in PbI_2 formation initiation time (see Figure 31c). This delay can be ascribed to the absence of moisture within ZnO film. In other words, by pre heating ZnO film, possible moisture that

can be entrapped within the porosities of ZnO film will be removed. Our results show the moisture accelerates the formation of perovskite in shorter annealing time. Previous study also suggests that perovskite film is extremely moisture-sensitive until fully crystallized [39].

However, shorter annealing time in turn means shorter subsequent over annealing time threshold when PbI_2 starts to form. Thus, to have better controlling on the procedures in the lab scale (ie. handling substrates to and from hot plate) it would be advantageous to make use of preheated ZnO films. Conclusively, favorable annealing time for H0 case is about 10s while it can be prolonged to about 30s for H1 case.

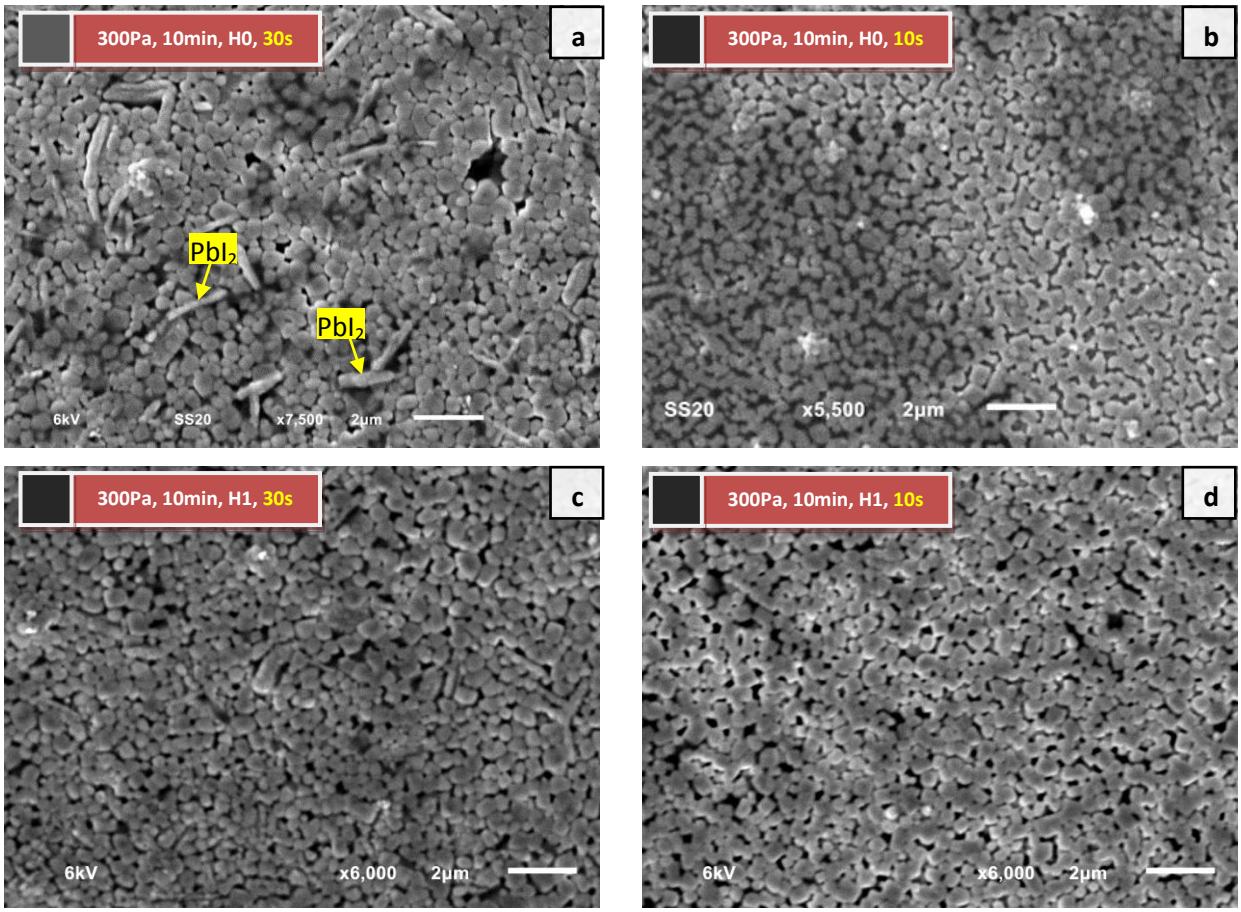

Figure 31: SEM images of perovskite after annealing on top of ZnO film (PLD fabricated at 300Pa for 10 min) at 100˚C for a) 30s, non preheated ZnO film, b) 10s, non-preheated ZnO film, c) 30s, preheated ZnO film d) 10s, preheated ZnO.

4-4-Cell fabrication based on optimized conditions

4-4-1-Double layer ZnO photoanode

Double layer structure (compact+porous film) was introduced to be beneficial to be exploited as the photoanode in solar cell fabrication. Compact layer serves as hole blocking layer and light harvesting and electron transportation are intended to be improved by porous layer.

According to film thickness/PLD duration proportionality lines (Thickness(nm) =14.698×Time(min) for 10Pa and Thickness(nm)=34.341×Time(min) for 300Pa), two types of double layer (DL) Structure were chosen to be fabricated as shown in Figure 32a and b. First, ~290nm-thick nanoporous film (deposited at 300Pa) on top of ~60nm-thick compact film (deposited at 10Pa), which hereafter is referred to as Thick-DL. Second, ~120nm-thick nanoporous film (deposited at 300Pa) on top of ~60nm-thick compact film (deposited at 10Pa), which hereafter is referred to as Thin-DL. Two different thicknesses were chosen for nanoporous film in order to probe the possible effect of ZnO film thickness on absorption spectra and final device efficiency.

In order to fabricate mentioned double layer structures, PLD process was carried out at 10 Pa oxygen pressure for 4.2min to deposit ~60nm-compact layer. In the same PLD run, once ~60nm-compact layer is completely deposited the oxygen pressure were increased with the rate of 6.5 Pa/s from 10Pa to 300Pa and kept constant for 2.6 and 8.5min to deposit the porous layers of 120 and 290nm thick, respectively.

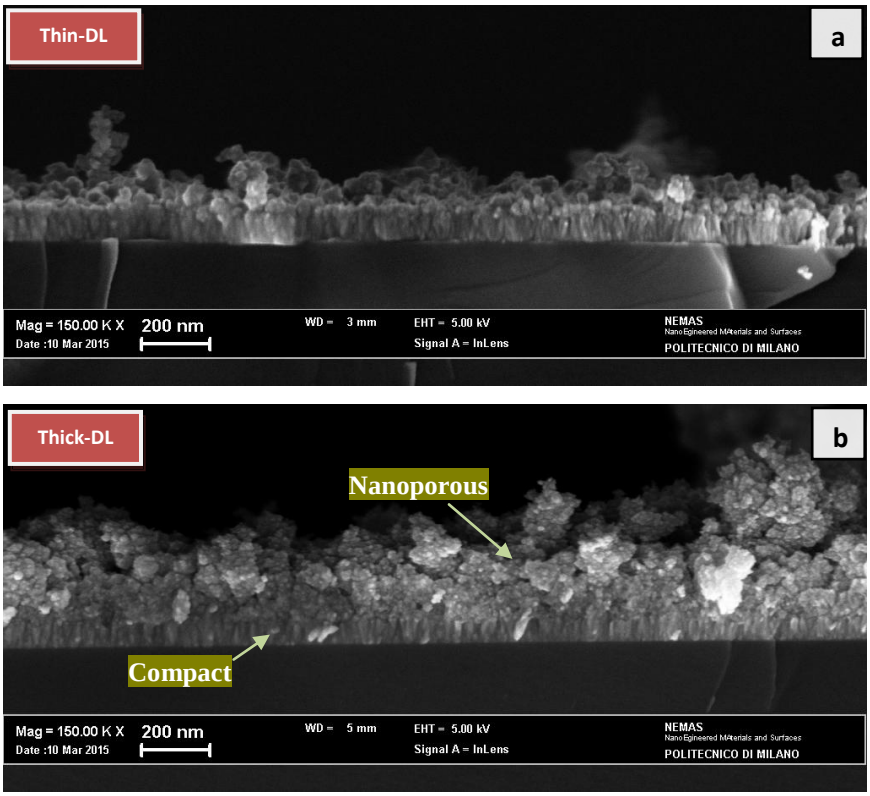

Figure 32: ZnO double layer structures made by ~60nm compact film and a) ~120nm b) ~290nm nanoporous film.

4-4-2-Annealing time optimization

Thin and Thick DL ZnO films were preheated at 120°C for 45min before perovskite spin coating to evaporate possible moisture within the pores. They were subsequently sensitized with perovskite and annealed at 100°C for 10, 15, 30 and 60s for thin-DL case and for 15 and 60s for thick-DL case (because of substrate limitations).

Figure 33 shows the SEM images of perovskite annealed at 100°C for 15 and 60 seconds on top of thin and thick DL ZnO films. Perovskite crystallites size, crystallites morphology and coverage are slightly different from previously shown microstructures (Figure 27 up to Figure 31). Figure 33b and d exhibit a microstructure consisting of rectangular-shape crystallites in the vicinity of colloids of small round-shape crystallites. The coverage, 80%, is also slightly lower than that of previously shown microstructures for similar ZnO film substrate, 84% (Figure 28).

The latter microstructure alteration can be attributed to slight human errors in perovskite precursor preparation. It is noteworthy that both previous and current perovskite precursors were prepared identically to obtain the same final precursor stoichiometry; of course slight variability in mixing different solutions or measuring the weight ratios are unavoidable. However, our findings in addition to personal communication with perovskite solar cell researchers state that these slight variations have an imperative impact on perovskite crystallites size and morphology, not on perovskite nominal chemical composition (confirmed by our optical density measurements). Likewise, previous study [6] also suggested that “due to the critical role of structural interactions of the perovskite organic/inorganic components, different crystallization/deposition methodologies can lead to crystals with identical nominal chemical composition but with different morphologies”.

In spite of above morphological discussion, trends discussed in chapters 4-2-1 and 4-3 in terms of ZnO thickness effect and annealing time turns out to be

consistent with current microstructures. In other words, Figure 33a and c show considerable presence of small pbI_2 rod-like crystallites (indicated by yellow arrows) after 60s annealing. Sample color is also shifted toward gray in presence of PbI_2. Moreover, comparing Figure 33a and c as well as Figure 33b and d, we can conclude that ZnO film thickness alteration does not change the crystallites size, crystallites morphology and coverage, consistent with previous observations.

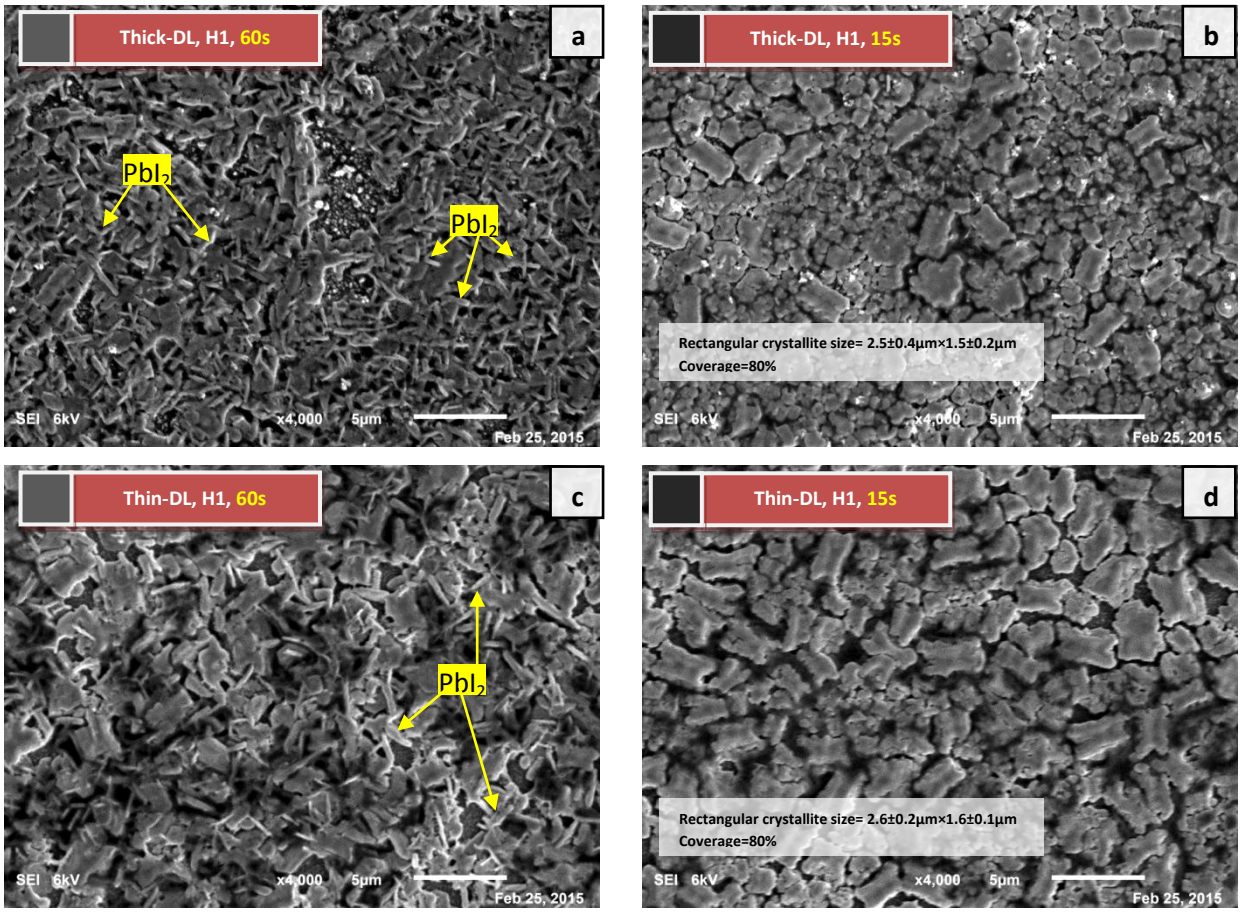

Figure 33: Top view SEM images of perovskite after annealing on top of ZnO film at 100˚C for a) 60s, Thick-DL, b) 15s, Thick-DL, c) 60s, Thin-DL d) 15s, Thin-DL.

4-4-2-1-Optical properties

4-4-2-1-1-PL intensity

So far, rods like crystallites were considered as PbI_2 and deleterious if formed in large amount. To confirm if rod-like crystallites are PbI_2, we measured the Raman spectra of perovskite sensitized ZnO films (Thin-DL) annealed at 100°C for both 15 and 60s case.

Raman spectra in 40-340cm^{-1} range showed only peaks corresponding to perovskite compound for both substrates similar to one shown in Figure 27b. In other words, PbI_2 associated peaks could not be detected in substrate annealed for 60s. The reason roots into intense photoluminescence of perovskite compound (band gap=770nm) once irradiated by green-light Raman laser (523nm) used in our spectroscopy. Photoluminescence of perovskite is so intense that obscures any other peaks associated to any other materials present in the substrate including PbI_2 and ZnO. It would be advantageous if we had implemented X-ray analysis to detect PbI_2.

However, photoluminescence (PL) results, presented in Figure 34, can be an indirect verification of PbI_2 presence. That is, PL intensity (around perovskite band gap) is proportional to perovskite volume fraction in the substrate. Since the only variable is annealing time and all other variables (including initial amount of spin coating perovskite precursor) remained unchanged, it can be concluded that lower PL of over annealed substrates (60s) is attributed to lower perovskite volume fraction in the expense of transformation into PbI_2.

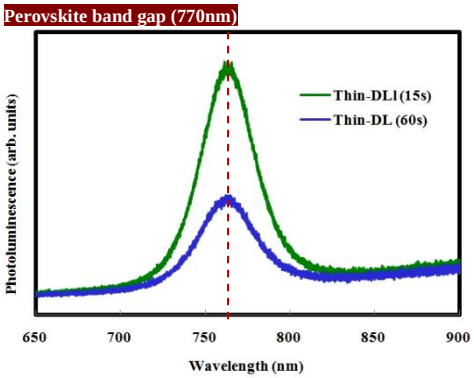

Figure 34: PL spectra of perovskite sensitized ZnO films (Thin-DL) annealed at 100°C for 15 and 60 seconds.

4-4-2-1-2-Absorption spectra

So far, samples' black coloration was considered as a criterion to approximate the degree of visible light absorption. Our photo-spectroscopy results confirm the latter approximation.

Optical density (OD) graphs for perovskite sensitized ZnO films (Thin-DL) annealed at 100˚C for 10, 15, 30, 60 seconds are shown in Figure 35. Dot-line refers to OD of thin-DL substrate without perovskite sensitization. Absorption spectra's trend and value exhibited by our samples are consistent with typical perovskite's one presented in the literature [41] and [6]. Within 400-1100nm range, highest absorption intensity found to be at 400nm; by moving toward larger wavelengths, there is a steep absorption decrease (400-450nm) followed by a smooth absorption decrease up to the bang gap. Around perovskite bang gap (770nm) absorption drops quite sharply. Ideally one should expect narrower transition around band gap for perfectly crystallized components, whereas the perovskite film of our samples may contains multiple structural defects so sub bands are likely to be present leading to about ±15nm transition range around the band gap at 770nm.

As discussed before, when annealing duration of perovskite sensitized ZnO film passes a certain time (annealing/over-annealing threshold), sample's color shifts from black to gray. The latter implies decrease in visible spectrum absorption confirmed by absorption spectra presented in Figure 35.

However, it is crucial to obtain a reliable annealing-time range in order to fabricate cells in a reproducible way according to highest absorption range. This annealing-time range, within which absorption spectra remains unchanged, was found to be any time between ~10s to ~20s for perovskite sensitized ZnO films (both thin and thick DL) annealed at 100˚C. Favorable annealing range and samples' actual images are shown in Figure 36. To fabricate final device in the next step of this project, 15s at 100˚C was chosen as optimized annealing condition.

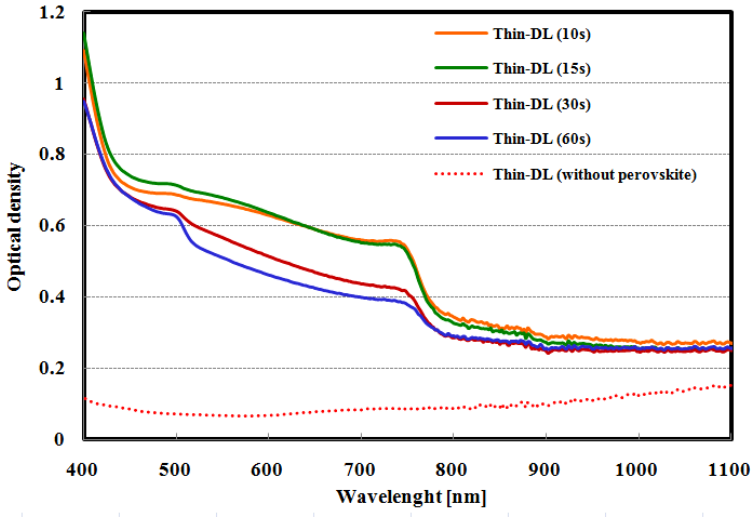

Figure 35: Absorption spectra of perovskite sensitized ZnO substrates (Thin-DL) annealed at 100°C for 10, 15, 30, 60 seconds.

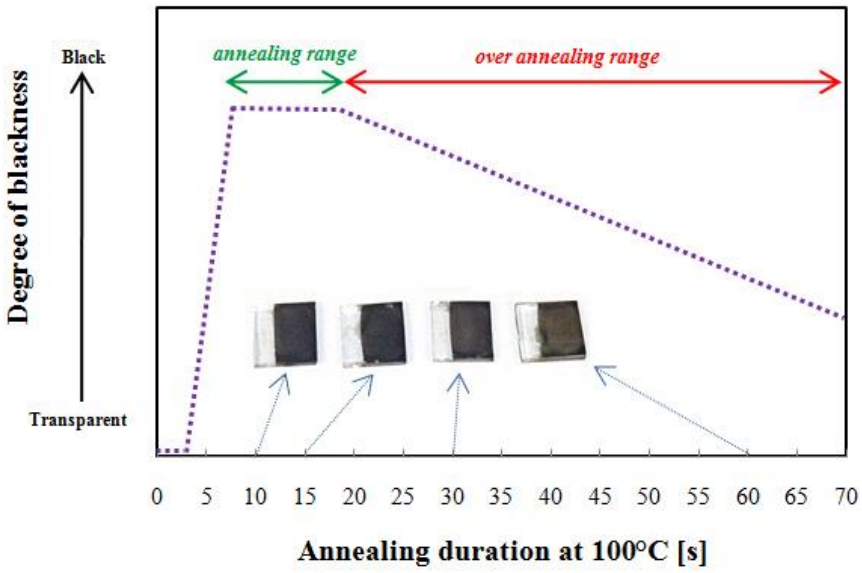

Figure 36: The schematic illustration of annealing time/blackness dependence.

Alteration in photoandoe characteristics is believed to affect absorption spectra of substrates even if other variables are remained unchanged. Gondoni et al. [9] have shown that the optical density of PCPDTBT deposited on the mesoporous AZO is significantly increased (up to 100%) in the 400–600 nm region with

respect to the compact one. This corresponded to an increase in light harvesting efficiency from 36% to 60% in the short wavelength absorption peak. Our findings, Figure 37, also suggest higher optical density for perovskite sensitized Thick-DL ZnO compared to that of Thin-DL. This can be attributed to the fact that Thick-ZnO film itself (without perovskite) absorbs light stronger than Thin-ZnO film (without perovskite) as dot lines indicate. For a given ZnO substrate, optical density decreases when annealing time increases from 15s to 60s.

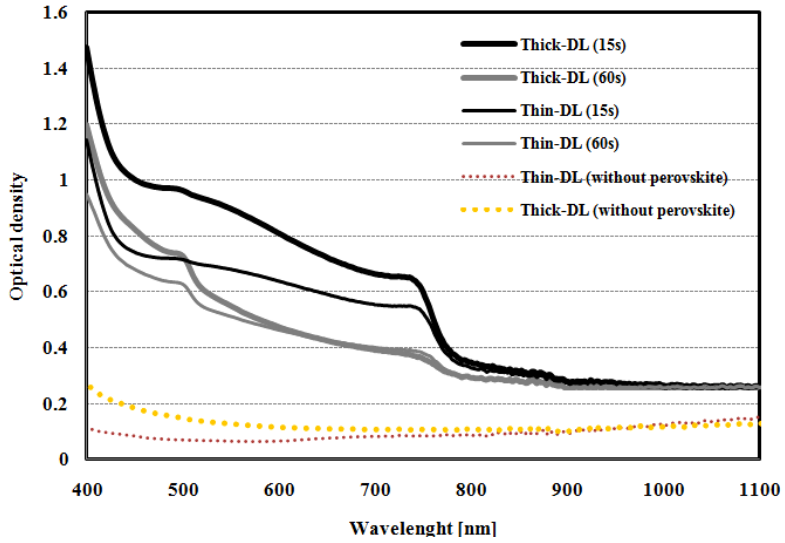

Figure 37: Absorption spectra of perovskite sensitized and non-sensitized ZnO films (Thin and Thick DL) annealed at 100˚C for 15 and 60 seconds.

4-4-3-Device efficiency

All investigations so far were aimed to propose the cell fabrication optimized protocol, 10 and 300Pa oxygen pressures as optimized pressures for favorable double layer structure as well as 15s perovskite annealing time at 100˚C as the optimized annealing duration to achieve highest visible range optical density.

We have made a few complete-architecture devices in order to verify (through solar simulator efficiency measurements) the feasibility of device realization. Nonetheless, superior efficiencies were already not anticipated since it requires finely tuning of multiple variables especially for such new emerging perovskite based solar cells whose fabrication protocol is updated day by day.

As represented in Figure 38a and b, the stack of device layers is as follows:

Glass/ FTO(600nm)/ compact-ZnO(~60nm)/ porous-ZnO/ perovskite(~700nm)/ Spiro(~190nm)/ Gold(~80nm).

Devices were fabricated on fluorine-doped tin oxide (FTO) coated glass. Initially FTO was removed by etching from regions under the anode contact, to prevent shunting upon contact with measurement pins. Substrates were then cleaned sequentially in 2% hallmanex detergent, acetone, propan-2-ol and oxygen plasma. Subsequently, both thin and thick double layer structures were deposited by PLD to probe the effect of their different absorption spectra on the final efficiency.

To form the perovskite layer, the non-stoichiometric precursor was spin-coated on the substrate in a nitrogen- filled glovebox, at 2000 rpm for 60s. Perovskite sensitized substrates were then annealed on a hotplate in the glovebox at 100˚C for 15 seconds. An experimental optimization of devices suggested PVK thicknesses between 400 and 800 nm were suitable for attaining high efficiency devices [39]. That is, perovskite thickness of 700nm (adopted in this project) is a balance between full photon absorption and electron and hole-diffusion length throughout the bulk perovskite.

A hole-transporting layer was then deposited in air via spin-coating a 0.79 M solution of 2,2′,7,7′-tetrakis-(N,N-di-p- methoxyphenylamine)9,9′-spirobifluorene

(spiro-OMeTAD) in chlorobenzene, with additives of lithium bis(trifluoromethanesulfonyl)imide and 4-tert-butylpyridine. Spin-coating was carried out at 2000 rpm for 60 s. Devices were then left overnight in air for the spiro-OMeTAD to dope via oxidation. Finally, 80 nm gold electrodes were thermally evaporated under vacuum of ≈10^{-6} Torr, at a rate of ≈0.1 $nm.s^{-1}$, to complete the devices.

The ultimate device architecture (top and cross section views), before measuring the efficiency by solar simulator, is shown in Figure 38c. For each device (1.4cm × 1.4cm) there exist 3 pixels (0.2cm × 0.7cm) which are thought as independent cells for independent efficiency measurements. In other words, in ideally homogenous and smooth structure throughout the device surface area (1.4cm × 1.4cm), 3 pixels should give rise to an equal efficiency. However, there are often minor differences in three pixel efficiencies possibly due to inhomogeneities associated with spin coating process.

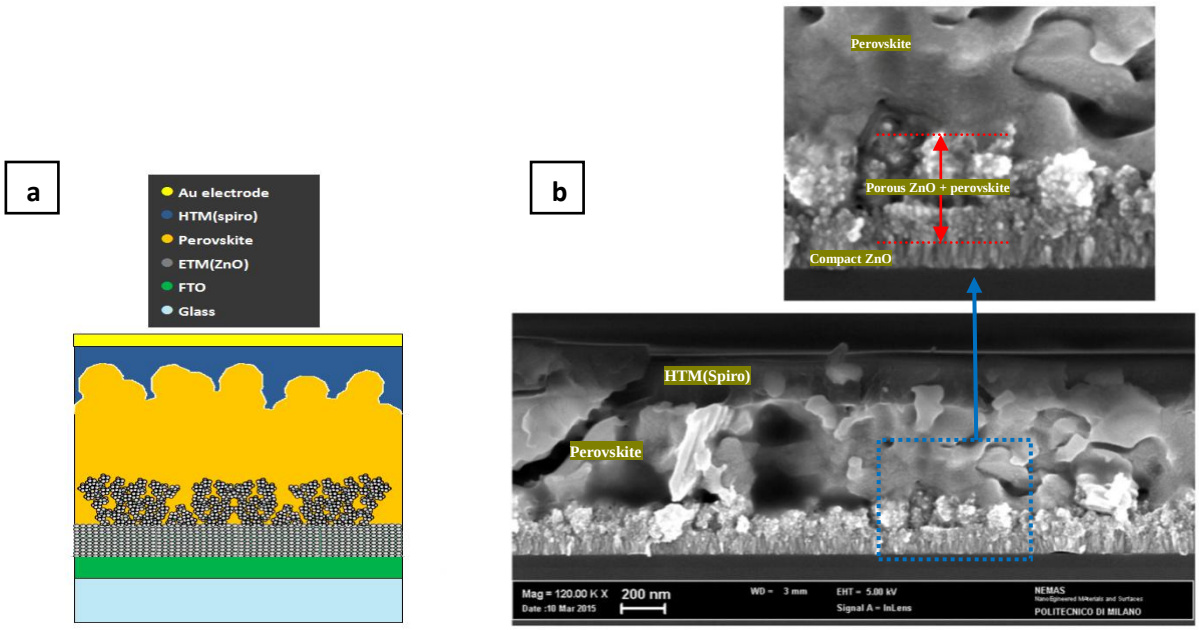

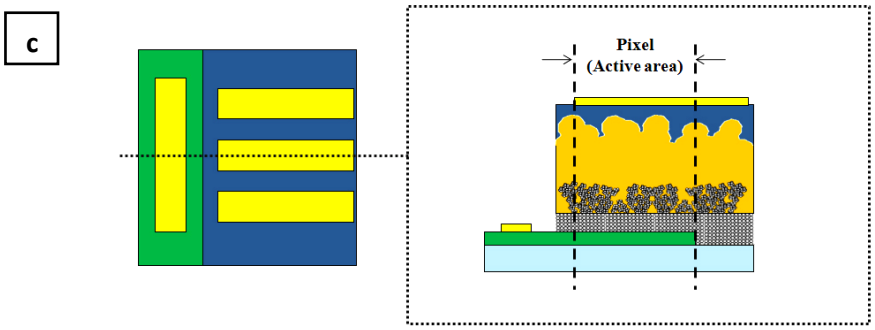

Figure 38: device stack of layers a) represented schematically b) shown by cross section SEM image [compact-ZnO/ Perovskite infiltrated porous-ZnO/Perovskite capping layer/Spiro]; c) ultimate device architecture for efficiency measurement.

Efficiencies for both thin and thick-DL adopted cells were measured according to the standard protocol, under simulated Air Mass (AM)1.5 full sun illumination. We managed to make only one thick-DL device (due to ZnO substrate limitation) which was not performing as a diode possibly due to an unintentional fabrication process inaccuracy.

On the other hand, thin-DL cell was performing as a diode in spite of its weak performance. The power conversion efficiencies (PCE) for 3 pixels of thin-DL device measured to be 0.60%, 0.92% and 0.59%, as presented in Table 2. The most efficient pixel (see Figure 39) is the central-region pixel where structure is likely to be more homogenous when implementing spin coating for layer depositions. 0.92% is still so far from 15.7% efficiency record for similar solar cell, ITO/ZnO/$CH_3NH_3PbI_3$/spiro-OMeTAD/Ag [3]. However, in order to systematically determine how low/high a cell efficiency can be considered, it must be compared with the standard cell. The standard cell (a well established cell architecture with known efficiency) must be fabricated along with the target new cells in order to normalize the process variations which may arise from each round of fabrication processes or from a laboratory to another laboratory. Unfortunately, we did not manage to fabricate the standard cell.

Table 2: Device parameters for three pixels of Thin-DL solar cell.

Pixel name	V_{OC} (V)	J_{SC} (mA/cm²)	P_{max} (mW)	Fill Factor (%)	PCE (%)	R_{Shunt} (Ohms)
1	0.63	5.68	0.03	16.87	0.60	15753.09
2	0.59	7.88	0.05	19.66	0.92	530106.9
3	0.61	4.94	0.03	19.61	0.59	111246.3

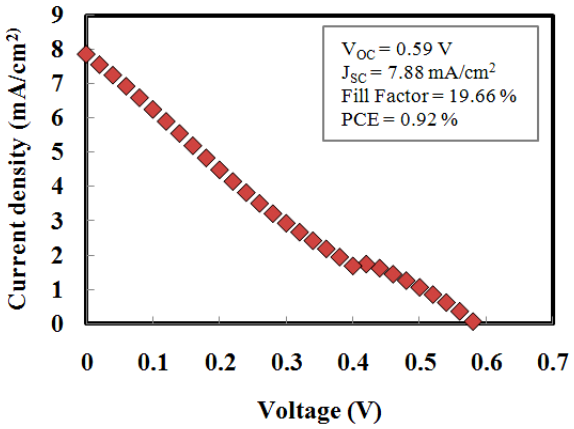

Figure 39: J–V characteristics for the highest-performing solar cell (central pixel), FTO/Thin-DL ZnO/Perovskite/Spiro/Au, measured under 100 mW/cm² , AM1.5G illumination.

The very low PCE (η) exhibited by our cells results from low value fill factor (FF), open-circuit voltage and short-circuit current density according to the following formula:

$$\eta = \frac{P_{\max}}{P_{in}} = \frac{J_{mp} V_{mp}}{P_{in}} = \frac{J_{sc} V_{oc} FF}{P_{in}}$$

We speculate that these low values are obtained as a result of unfavorable perovskite stoichiometry and coverage or gold/FTO interface.

The perovskite pigment has been deposited in a single step onto nanoporous ZnO films using a mixture of PbI_2 and CH_3NH_3I in a common solvent. Upon spin-coating, an organic and halide-rich film is formed. As the thermal annealing process takes place, it is likely to be energetically favorable for the excess

organic and halide to evaporate, once a temperature threshold is reached. This would continue until a crystal with equimolar amounts of organic, metal and halide (1:1:3 organic:metal:halide by moles) is left [39].

However, previous study [26] suggests that one-step deposition is associated with uncontrolled precipitation of the perovskite producing large morphological variations and correspondingly wide spread of photovoltaic performance in the resulting devices. In other words, we speculate that only 15s annealing perovskite at 100°C is not thermodynamically sufficient to achieve the stoichiometry of 1:1:3 organic:metal:halide by moles. Therefore, possible excessive organic compound can be remained resulting in carrier entrapment. We might need to optimize the annealing duration for a lower annealing temperature than 100°C enabling perovskite to form gradually resulting in a desirable stoichiometry.

Moreover, it was suggested by previous study that the highest photocurrents are attainable only with the highest perovskite surface coverages [39]. The 80% perovskite coverage of our cells might not be sufficient for a high-performing cell. The effects of poor coverage are twofold: firstly, if there are regions of no perovskite coverage, light will pass straight through without absorption, decreasing the available photocurrent; secondly, insufficient coverage results in a high frequency of "shunt paths" allowing contact between spiro-OMeTAD and the TiO_2 compact layer. Any such contact will act as a parallel diode in the solar cell equivalent circuit, causing a drop in V_{oc} and fill factor, and accordingly power conversion efficiency [39].

The sequential two-step deposition which was introduced on July 2013 [26] and is being recently adopted as the protocol to high-performance PerovCells may most probably overcome the perovskite stoichiometry and coverage drawbacks discussed before. Two-step deposition is carried out as follows:

PbI_2 is dissolved in N,N-dimethylformamide at a concentration of 462mg ml^{-1} (~1 M) under stirring at 70°C. The solution is kept at 70°C during the whole procedure. The mesoporous photoanode films are then infiltrated with PbI_2 by

spin coating at 6,500r.p.m. for 90s and dried at 70°C for 30 min. After cooling to room temperature, the films were dipped in a solution of CH_3NH_3I in 2-propanol (10mg ml^{-1}) for 20s, rinsed with 2-propanol and dried at 70°C for 30 min.

However, it is noteworthy that while this project was being carried out one-step deposition was considered as the typical perovskite deposition protocol widely used by researchers even for perovskite sensitization of ZnO substrates [6]. So far, the most successful one-step method case is $CH_3NH_3PbI_{3-x}Cl_x$ which is well illustrated by Yang group with the cell PCE of 19.3% [42]. In addition to mentioned possible explanations for low PCE, we also believe that ultimate cell architecture, before efficiency measurements, was not ideally fabricated as should be done represented in Figure 38c. That is, after all layers are deposited subsequently from FTO, ZnO-compact, ZnO-porous, perovskite up to spiro, small area of all layers (except FTO) is typically scratched in order to expose FTO for subsequent gold electrode deposition. However, it was not done perfectly because compact ZnO film is so stable and adherent to its underneath FTO that couldn't be removed by simple scratching. Figure 40 shows schematically the actual ultimate cell architecture whose efficiency was measured by solar simulator. To overcome this problem, compact ZnO film must have been removed by selective ZnO solution etching at that particular area.

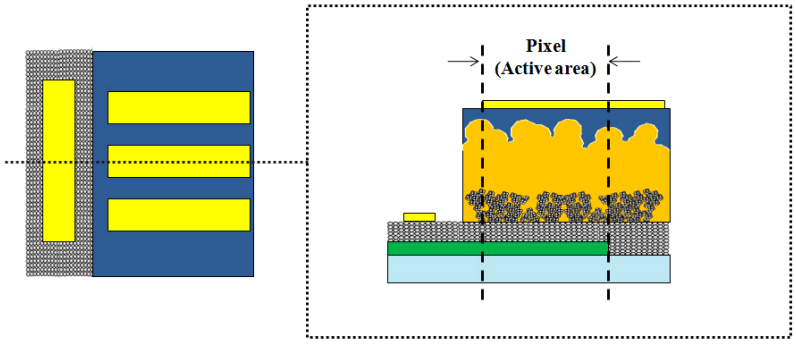

Figure 40: Schematic representation of actual ultimate device architecture before efficiency measurement.

All in all, even though our cells exhibited unfavorable operation, we believe there are many rooms for further investigations so as to overcome the possible proposed problems in the future works. To sum up, exclusively for one-step deposited perovskite on ZnO substrates a systematic study can be done to find the optimized annealing temperature (lower than 100˚C) and duration (longer than 15s) to form perfectly stoichiometric perovskite compound. Plus, high degree of accuracy must be adopted during different steps of cell fabrication especially for FTO/Gold interface contact. Standard cell is essential to be made along with target cells to normalize fabrication variations. Last but not least, identical batch of perovskite precursor must be exploited for systematic studies in order to have reproducible perovskite microstructure.

There is still a long way to go to meet the rigid requirement for long-term outdoor practical applications. Scientists anticipate that PCEs of 28 to 30% are feasible in the near future by fabricating perovskite and crystalline silicon cells in a tandem configuration [43].

5-Conclusions and perspectives

In this project, we systematically investigated the feasibility of PLD fabricated ZnO to be utilized as photoanode in the PerovCells. Unique potentials of ZnO as photoanode material presenting high electron mobility, its feasibility for flexible solar cell fabrication, significantly short perovskite annealing time necessity in addition to its similar vacuum energy levels with respect to the conventionally used photoanode, TiO_2, renders it an interesting candidate for large-scale PerovCell fabrication.

The state-of-the-art perovskite oriented stack of layers was chosen for cell fabrication, namely Glass/FTO/compact-ZnO/nanoporous-ZnO/Perovskite/Spiro/Au. A double layer structure (ie. a nanoporous layer on top of a compact layer) formed the ZnO photoanode architecture offering a combination of improved light harvesting and high electron transport in addition to blocking hole transport from perovskite to FTO.

Pulsed laser deposition parameters including deposition duration and background oxygen pressure were optimized to attain the favorable ZnO film thickness and degree of porosity, respectively. We demonstrated that 10 and 300Pa oxygen pressures are suitable to make the compact and nanoporous ZnO films, respectively.

In the next step, perovskite solution was spin coated on ZnO films and immediately annealed at 100˚C for various durations ranging from 10s to 60s. Our finding demonstrated that there exists an annealing time range as narrow as about 10s (from 10s to 20s) in order to form the desirable perovskite film. Accordingly, 15s annealing at 100˚C was selected to be the optimized annealing condition offering the highest volume fraction of perovskite crystallites (verified by PL result and SEM images) and highest visible light absorption (verified by optical density result). Our findings also suggested that increasing ZnO film thickness (keeping other variables constant) results in higher visible range

absorption even though perovskite crystallites morphology, size and film coverage are not influenced by ZnO film thickness.

Finally, ultimate device architecture was fabricated in order to evaluate cell performance through its J-V curve measured under 100 $mW.cm^{-2}$, AM1.5G illumination by solar simulator. The devices were made adopting optimized conditions, ie. double layer ZnO photoanode and perovskite annealing at 100°C for 15s. According to our J-V curve in addition to SEM, OD, PL and Raman results we related the cell operation to the fundamental properties of the constituent materials. The device was successfully operating as a solar cell even though its performance was not impressive. We also proposed a set of issues which can be further investigated in the future works to improve the cell performance. There is still a long way to go to meet the rigid requirement for long-term outdoor practical applications of perovskite based solar cells.

Bibliography

1. Bi, D., et al., *Effect of different hole transport materials on recombination in CH3NH3PbI3 perovskite-sensitized mesoscopic solar cells.* The Journal of Physical Chemistry Letters, 2013. **4**(9): p. 1532-1536.
2. Lee, M.M., et al., *Efficient hybrid solar cells based on meso-superstructured organometal halide perovskites.* Science, 2012. **338**(6107): p. 643-647.
3. Liu, D. and T.L. Kelly, *Perovskite solar cells with a planar heterojunction structure prepared using room-temperature solution processing techniques.* Nature Photonics, 2014. **8**(2): p. 133-138.
4. Peng, G., X. Xu, and G. Xu, *Hybrid Organic-Inorganic Perovskites Open a New Era for Low-Cost, High Efficiency Solar Cells.* Journal of Nanomaterials, 2014.
5. Zhang, Q., et al., *ZnO Nanostructures for Dye-Sensitized Solar Cells.* Advanced Materials, 2009. **21**(41): p. 4087-4108.
6. De Bastiani, M., et al., *Role of the crystallization substrate on the photoluminescence properties of organo-lead mixed halides perovskites.* APL Materials, 2014. **2**(8): p. 081509.
7. Green, M.A., A. Ho-Baillie, and H.J. Snaith, *The emergence of perovskite solar cells.* Nature Photonics, 2014. **8**(7): p. 506-514.
8. Sauvage, F., et al., *Hierarchical TiO2 photoanode for dye-sensitized solar cells.* Nano letters, 2010. **10**(7): p. 2562-2567.
9. Gondoni, P., et al., *Enhancing light harvesting by hierarchical functionally graded transparent conducting Al-doped ZnO nano-and mesoarchitectures.* Solar Energy Materials and Solar Cells, 2014. **128**: p. 248-253.
10. Hosenuzzaman, M., et al., *Global prospects, progress, policies, and environmental impact of solar photovoltaic power generation.* Renewable and Sustainable Energy Reviews, 2015. **41**: p. 284-297.
11. *Available from: The Renewable Energy Policy Network for the 21st Century (www.ren21.net).*
12. Zeman, M., *Introduction to photovoltaic solar energy.*
13. Green, M.A., *Third generation photovoltaics: Ultra-high conversion efficiency at low cost.* Progress in Photovoltaics: Research and Applications, 2001. **9**(2): p. 123-135.
14. Grätzel, M., *Dye-sensitized solar cells.* Journal of Photochemistry and Photobiology C: Photochemistry Reviews, 2003. **4**(2): p. 145-153.
15. Green, M.A., et al., *Solar cell efficiency tables (Version 45).* Progress in photovoltaics: research and applications, 2015. **23**(1): p. 1-9.
16. Turner, G., *Global Renewable Energy Market Outlook 2013.* Bloomberg New Energy Finance https://www. bnef. com/insightdownload/7526/pdf (11 April 2014), 2013.

17. Snaith, H.J., *Perovskites: the emergence of a new era for low-cost, high-efficiency solar cells.* The Journal of Physical Chemistry Letters, 2013. **4**(21): p. 3623-3630.
18. Anaya, M., et al., *Optical Description of Mesostructured Organic-Inorganic Halide Perovskite Solar Cells.* The Journal of Physical Chemistry Letters, 2015.
19. Baikie, T., et al., *Synthesis and crystal chemistry of the hybrid perovskite (CH 3 NH 3) PbI 3 for solid-state sensitised solar cell applications.* Journal of Materials Chemistry A, 2013. **1**(18): p. 5628-5641.
20. Ponseca Jr, C.S., et al., *Organometal halide perovskite solar cell materials rationalized: Ultrafast charge generation, high and microsecond-long balanced mobilities, and slow recombination.* Journal of the American Chemical Society, 2014. **136**(14): p. 5189-5192.
21. Etgar, L., et al., *Mesoscopic CH3NH3PbI3/TiO2 heterojunction solar cells.* Journal of the American Chemical Society, 2012. **134**(42): p. 17396-17399.
22. Heo, J.H., et al., *Efficient inorganic-organic hybrid heterojunction solar cells containing perovskite compound and polymeric hole conductors.* Nature Photonics, 2013. **7**(6): p. 486-491.
23. Kojima, A., et al. *Novel photoelectrochemical cell with mesoscopic electrodes sensitized by lead-halide compounds (2)*. in *Meeting Abstracts*. 2006. The Electrochemical Society.
24. Kojima, A., et al., *Organometal halide perovskites as visible-light sensitizers for photovoltaic cells.* Journal of the American Chemical Society, 2009. **131**(17): p. 6050-6051.
25. Kim, H.-S., et al., *Lead iodide perovskite sensitized all-solid-state submicron thin film mesoscopic solar cell with efficiency exceeding 9%.* Scientific reports, 2012. **2**.
26. Burschka, J., et al., *Sequential deposition as a route to high-performance perovskite-sensitized solar cells.* Nature, 2013. **499**(7458): p. 316-319.
27. Casari, C.S. and A.L. Bassi, *Pulsed laser deposition of nanostructured oxides: from clusters to functional films.* Advances in laser and optics research. Nova Science Publishers Inc., New York, 2012: p. 65-100.
28. Eason, R., *Pulsed laser deposition of thin films: applications-led growth of functional materials*. 2007: John Wiley & Sons.
29. Itina, T., W. Marine, and M. Autric, *Mathematical modelling of pulsed laser ablated flows.* Applied surface science, 2000. **154**: p. 60-65.
30. Amoruso, S., et al., *Propagation of LaMnO 3 laser ablation plume in oxygen gas.* Applied surface science, 2006. **252**(13): p. 4712-4716.
31. Arnold, N., J. Gruber, and J. Heitz, *Spherical expansion of the vapor plume into ambient gas: an analytical model.* Applied Physics A, 1999. **69**(1): p. S87-S93.
32. Atkins, P., *Shriver and Atkins' inorganic chemistry*. 2010: Oxford University Press.

33. Grancini, G., et al., *The Impact of the Crystallization Processes on the Structural and Optical Properties of Hybrid Perovskite Films for Photovoltaics.* The Journal of Physical Chemistry Letters, 2014. **5**(21): p. 3836-3842.
34. Norrman, K., A. Ghanbari-Siahkali, and N. Larsen, *6 Studies of spin-coated polymer films.* Annual Reports Section" C"(Physical Chemistry), 2005. **101**: p. 174-201.
35. Kusuhara, M., *Solar simulator*. 1987, Google Patents.
36. *Available from: www.globalwarmingart.com.*
37. Bailini, A., et al., *Pulsed laser deposition of tungsten and tungsten oxide thin films with tailored structure at the nano-and mesoscale.* Applied surface science, 2007. **253**(19): p. 8130-8135.
38. Ohtomo, A. and A. Tsukazaki, *Pulsed laser deposition of thin films and superlattices based on ZnO.* Semiconductor science and technology, 2005. **20**(4): p. S1.
39. Eperon, G.E., et al., *Morphological Control for High Performance, Solution-Processed Planar Heterojunction Perovskite Solar Cells.* Advanced Functional Materials, 2014. **24**(1): p. 151-157.
40. Chen, Q., et al., *Controllable self-induced passivation of hybrid lead iodide perovskites toward high performance solar cells.* Nano letters, 2014. **14**(7): p. 4158-4163.
41. D'Innocenzo, V., et al., *Excitons versus free charges in organo-lead tri-halide perovskites.* Nature communications, 2014. **5**.
42. Zhou, H., et al., *Interface engineering of highly efficient perovskite solar cells.* Science, 2014. **345**(6196): p. 542-546.
43. Ball, J.M., et al., *Low-temperature processed meso-superstructured to thin-film perovskite solar cells.* Energy & Environmental Science, 2013. **6**(6): p. 1739-1743.